Planetary-Scale Waves and the Cyclic Nature of Cloud Top Dynamics on Venus

ANTHONY D. DEL GENIO AND WILLIAM B. ROSSOW

NASA/Goddard Space Flight Center, Institute for Space Studies, New York, New York

(Manuscript received 1 January 1989, in final form 3 August 1989)

ABSTRACT

Pioneer Venus OCPP ultraviolet images spanning eight years have been analyzed objectively to derive quantitative information on the properties of planetary-scale wave modes at the Venus cloud tops. We infer propagation characteristics for longitudinal wavenumber 1 by Fourier analyzing time series of longitudinal mean normalized image brightness. The dominant equatorial mode during 1979–80 was the 4-day periodicity associated with zonal motion of the *Y*-feature. The difference between this and the 4.7-day equatorial rotation period derived from the tracking of small cloud features implies that the *Y* is a propagating wave with a prograde phase speed of about 15 m s^{-1} relative to the wind. Simultaneous time series of cloud-tracked wind fluctuations also exhibit a 4-day periodicity, lending support to the wave interpretation. The prograde propagation and equatorial confinement of the wave, and the absence of analogous meridional wind fluctuations, identify it as a Kelvin wave. Zonal winds peak near the leading edge of the *Y*; gravity wave theory then implies that dark UV features at low latitudes are cold and produced by upwelling or convection associated with the wave. In 1982–83 the Kelvin mode was very weak or absent, replaced by a 5-day equatorial periodicity in brightness that is not significantly different from the 5.0-day cloud-tracked wind rotation period recorded during those years. Zonal wind fluctuations for 1982 show no obvious spectral peak, suggesting that brightness variations at this time are due to advection of a remnant albedo pattern rather than active wave propagation. The Kelvin wave amplitude and implied propagation characteristics suggest that it dissipates at the cloud tops and contributes significantly to the maintenance of the cloud top equatorial superrotation. The disappearance of the Kelvin wave between 1980 and 1982 may therefore explain the coincident 5–10 m s^{-1} decline in the equatorial zonal wind. The 1985–86 images indicate a return of the 4-day brightness periodicity and a restoration of equatorial wind speeds similar to those in 1979–80. Thus, the cloud level dynamics may be cyclic, with an apparent time scale of 5–10 years. A separate midlatitude planetary-scale transient mode with a period near 5 days also occurs when the 4-day equatorial wave is present. The midlatitude mode retrogrades with respect to the zonal wind and may be a slowly rotating analog to an internal Rossby–Haurwitz wave generated by shear instability of the midlatitude jet. If so, it too may accelerate the equatorial wind. Solar-locked diurnal and semidiurnal tidal modes are also present in both the brightness and cloud-tracked wind data during all imaging periods; their amplitudes appear to be similar to that of the equatorial Kelvin wave. The long-term evolution and maintenance of the Venus cloud top superrotation may therefore reflect a complex balance among at least four eddy momentum transport mechanisms.

1. Introduction

The superrotation of the Venus atmosphere is one of the most puzzling phenomena known to planetary fluid dynamicists. The spatial and temporal distribution of the zonal winds has now been fairly well documented by a variety of Pioneer Venus experiments, including differential long baseline interferometry (DLBI) observations of the descent probes (Counselman et al. 1980), tracking of UV cloud features in Orbiter Cloud Photopolarimeter (OCPP) images (Limaye et al. 1982, 1988; Rossow et al. 1980, 1989), and cyclostrophic thermal wind reconstructions of Orbiter Infrared Radiometer (OIR) and radio occultation temperature fields (Schofield and Taylor 1983; Newman et al. 1984; Walterscheid et al. 1985). Doppler tracking of numerous Venera probes (cf. Kerzhanovich and Marov 1983; Limaye 1985) and the VEGA balloons (Preston et al. 1986) provides additional evidence for the prevalence of strong zonal winds at and below the cloud tops. A fully self-consistent theory of the superrotation has yet to emerge, however.

The midlatitude jet observed at the cloud tops in these datasets is the result of poleward advection of angular momentum by a Hadley cell driven by solar heating in the clouds. This aspect of the circulation has been simulated in numerous models (Rossow 1983; Covey et al. 1986a; Del Genio and Suozzo 1987; Williams 1988). The strong *equatorial* zonal winds present at all altitudes are the real crux of the superrotation problem. These cannot be produced by a purely axisymmetric circulation, so eddy angular momentum transports are required (cf. the review by Rossow 1985). Several mechanisms for generating such eddies have been proposed: 1) barotropic instability of the

Corresponding author address: Dr. Anthony D. Del Genio, NASA/GSFC, Institute for Space Studies, 2880 Broadway, New York, NY 10025.

midlatitude jet (Gierasch 1975; Rossow and Williams 1979); 2) solar-locked thermal tides or "moving flame" circulations (Young and Schubert 1973; Fels and Lindzen 1974; Pechmann and Ingersoll 1984; Covey et al. 1986b; Leovy 1987); and 3) transient or topographically forced planetary- or small-scale gravity waves (Leovy 1973; Hou and Farrell 1987; Gierasch 1987).

To assess the relative importance of these mechanisms, observations of the eddies are needed. Evidence for waves exists in Pioneer Venus OIR data (Taylor et al. 1980; Elson 1983) and VEGA balloon Doppler tracking measurements (Young et al. 1987), but both of these are limited in their temporal coverage. The only long-term spacecraft record of dynamic variability at low latitudes on Venus comes from the Pioneer Venus OCPP experiment (Travis et al. 1979). OCPP provides information relevant to the dynamics at cloud levels in the form of cloud-tracked winds and UV cloud albedo patterns (Rossow et al. 1980, 1989). Direct information on transient eddies can be obtained by Fourier analyzing time series of wind fluctuations when a sufficiently long continuous record exists. At other times, wavelike features can still be detected indirectly via Fourier analysis of analogous time series of UV brightness variations. The potential of this technique has already been demonstrated in a study of Pioneer Venus nominal mission image data (Del Genio and Rossow 1982). Stationary eddies can be resolved in either wind or brightness data by averaging in an appropriately fixed coordinate system.

The advantage of deriving eddy information from UV brightness variations as opposed to wind variations is the more comprehensive nature of the former dataset. Brightness values are defined for every pixel in every image, and when normalized to remove scattering geometry effects, the errors in individual pixel values are small except near the limb and terminator. The disadvantage of the brightness data is the ambiguity involved in interpreting the observed variations in terms of fluctuations in meteorological quantities. Cloud-tracked wind vectors, on the other hand, can be interpreted directly. However, they are available only when pairs of images are acquired on the same orbit and are sparsely and irregularly spaced over the disk. Furthermore, the errors associated with individual wind measurements reduce the signal-to-noise ratio in the power spectrum. We therefore use the brightness record as our primary means to detect waves and the wind record to validate the results when feasible and to provide physical interpretations.

Understanding the nature of the UV features really involves two separate issues: the chemical identity and vertical distribution of the material responsible for UV absorption, and the physical mechanisms that cause its concentration to be horizontally inhomogeneous so as to produce the patterns seen in OCPP images. SO_2 has been identified as the dominant UV absorber at wavelengths < 320 nm but cannot account for the features at the 365 nm wavelength of the OCPP images. SO_2 is spatially correlated with dark regions at 365 nm, however, and may therefore be involved in the process that produces the second UV absorber (Esposito 1980; Esposito and Travis 1982). The decrease in contrast with increasing phase angle in OCPP images and the cloud top refractive index consistent with OCPP polarimetry analyses imply that the 365 nm absorber is embedded within the main sulfuric acid cloud (Travis et al. 1979). Chemical–microphysical models of the Venus clouds, under conditions of O_2 depletion, produce forms of elemental sulfur whose optical properties match the requirements for the unknown absorber (Toon et al. 1982). However, the specific sulfur allotropes are open to question (Young 1985), and other candidates for the absorbing material may also be viable (Hartley et al. 1989). Furthermore, the use of a continuum model instead of a band model for SO_2 absorption may introduce errors in the derived abundance and vertical profile of SO_2, which can affect the range of acceptable chemical models (Belton 1982). Thus, the identity and precise location of the UV absorber are still open to question.

The physical nature of UV albedo contrasts is somewhat better understood. Variations in the height of the main sulfuric acid cloud and thickness of the overlying submicron haze are too small to account for much of the contrast, except for some of the differences in appearance between the equatorial and polar regions (Travis 1975; Esposito and Travis 1982). Horizontal variations in the cloud top concentration of the UV absorber are probably responsible for most of the contrast. A number of workers have proposed that dark regions are produced by upwelling motion or vertical turbulent mixing, which brings the embedded absorber closer to the visible cloud top (Crisp and Young 1978; Esposito and Travis 1982; Toon et al. 1982). The detailed correlations between dark regions and other variables have not yet been established, though. One problem with the upwelling hypothesis is the maintenance of distinct UV patterns in the face of turbulent mixing, which would tend to produce a uniformly dark scene. To explain the observed contrasts, the time scale for eddy diffusion must exceed the time scale for production and removal of the UV absorber. Sedimentation times for the cloud particles are too long (Rossow 1978). This implies that either the chemical lifetime of the absorbing material (Toon et al. 1982) or the vertical advection time for transport of the absorber, or both, are short.

The eight-year OCPP dataset enables us to establish a climatology of both the mean flow and planetary-scale waves at the cloud tops, including temporal changes. In order to interpret the long-term variations we see as a true temporal evolution of the dynamics, we must address the question of whether the altitude we see in the images is variable in space and time rather

than the dynamics. In the equatorial region the optical depth τ of the submicron haze above the main cloud is ≤ 0.1 (Kawabata et al. 1980), so the 1 μm sulfuric acid droplets and UV absorber are totally responsible for the UV features there. For the main cloud in the polarimetry analysis, $\tau = 1$ occurs at about 30 mb (70 km). The features we see in low latitudes must lie primarily below this level and above about 100 mb (65 km), corresponding to $\tau \sim 5$ in data from the Large Probe Cloud Particle Size Spectrometer and Solar Flux Radiometer (Knollenberg et al. 1980). Long-term variations in equatorial cloud-tracked winds are of order 5–10 m s^{-1} (Limaye et al. 1982, 1988; Rossow et al. 1989). The vertical shear at the equator at 65–70 km has not been measured directly, and cyclostrophic balance estimates are not precise near the equator. However, the mean meridional temperature gradient at low latitudes appears to change sign at these levels (Schofield and Taylor 1983; Newman et al. 1984), suggesting that the UV cloud level is near the altitude of maximum zonal wind. We estimate a thermal wind shear of ≤ 1–2 m s^{-1} km^{-1} from cyclostrophic balance calculations at 65–70 km and 15°–20° latitude (Newman et al. 1984). The cloud top altitude would therefore have to change by a scale height or more over the course of the mission to explain the observed temporal wind variations at the equator. This is larger than observed long-term variations of the $\tau = 1$ level (Coffeen and Hansen 1974; Hansen and Hovenier 1974; Kawabata et al. 1980). Furthermore, changes in cloud height are likely to be accompanied by comparable shifts in the position of peak wind. We tentatively conclude that most of the temporal variability of the flow in our equatorial data is real. A definitive assessment awaits future analysis of OCPP polarimetry data, however.

The situation at higher latitudes is different for three reasons. We view these regions at higher slant angles and the submicron haze $\tau \approx 0.8$ (Kawabata et al. 1980), both of which suggest less penetration of the solar flux and a contribution of the haze to UV contrast there. On the other hand, the main cloud top is some 10 mb deeper than in the equatorial region (Kawabata et al. 1980), which may partially offset this effect if the vertical distribution of UV absorber is not similarly shifted downward at these latitudes. The height of cloud unit optical depth in the infrared varies with latitude by ≤ 1 km except near the pole (Schofield and Taylor 1983). Thus, latitudinal variations seen in the OCPP data are affected little by cloud-height bias. Significant changes in haze optical depth poleward of 70° latitude are observed on the 1–2 month time scale (Travis et al. 1989). Therefore, high-latitude temporal variations in dynamical quantities must be viewed circumspectly. Oscillations in brightness and wind, however, appear to be centered no further poleward than 40°–50°, where haze variability is probably of less concern. We will show, furthermore, that dynamical fluctuations at low and high latitudes seem to be correlated, thus arguing for the reality of the latter.

In this paper we use the analysis procedure of Del Genio and Rossow (1982) to examine short-term temporal variations of wind and UV brightness over eight years of OCPP imaging and relate them to long-term wind variations (Rossow et al. 1989). We demonstrate that transient and stationary planetary-scale waves can be detected in both datasets and identified as particular wave modes. This identification, along with observed correlations between fluctuations in wind and brightness, determines the process that gives rise to the UV features and permits an interpretation of these contrasts in terms of standard meteorological quantities (as assumed by Del Genio and Rossow). This in turn allows us to assess the relative importance of various modes in contributing to the cloud top superrotation.

The paper is organized as follows. We describe the OCPP dataset and analysis technique in section 2. Sections 3 and 4 contain the results of our time series analyses of brightness and wind fluctuations, respectively, as well as comparisons between the two, and our identification of transient wave modes. Solar-fixed waves in the data are discussed in section 5. In section 6 we discuss possible forcing mechanisms for these waves and the implications of our results for understanding the superrotation of the cloud level atmosphere of Venus. Our concluding remarks are in section 7.

2. Dataset and analysis technique

OCPP images are acquired during the long apoapsis portion of the elliptical Pioneer Venus orbit by a spin-scan technique, which requires about 4 h for the generation of a single full-disk image (Travis 1979). A maximum of four full-disk images can be acquired on a single 24-h orbit; complementary polarimetry observations and the requirements of other Pioneer Venus instruments often limit us to fewer than this number. Image analysis demands that a substantial fraction of the disk be illuminated, since UV contrasts decline rapidly at high phase angles (Travis et al. 1979). Since the Pioneer Venus orbit is fixed in inertial space, useful imaging can therefore occur for no longer than about three months out of every Venus year, when the sun–planet–spacecraft phase angle is $\leq 60°$. Availability of the Deep Space Network for telemetry coverage and data rate variations over the Venus synodic period further restrict image acquisition.

The net result is that over the lifetime of the Pioneer Venus Orbiter we have obtained five "good" imaging datasets, each with 2–3 months of relatively uninterrupted coverage, and three shorter datasets of about 1 month duration. The detailed characteristics of the data in each of these imaging periods are summarized in Table 1. (To be usable for time series analysis, we require long sequences of at least one image per day,

TABLE 1. Characteristics of the image datasets used in this study.

Imaging epoch	Days of year	Length (days)	Days missing	No. of images
Spring 1979	7–72	66	0	119
Fall 1979	283–309	27	8	32
Spring 1980	88–166	79	0	282
Spring 1982	35–113	79	0	276
Fall 1982	258–284	27	6	39
Spring 1983	121–199	79	12	158
Spring 1985	73–141	69	13	78
Summer 1986	195–229	35	13	36

with few gaps. The data in Table 1 therefore differ slightly from those used for cloud tracking [Table 1 of Rossow et al. 1989], which requires pairs of images but is not constrained by gaps in imaging coverage.) A total of 1,020 images were analyzed for this paper. The spring 1980 and spring 1982 imaging periods are by far the most comprehensive, with at least one image available for every day in the dataset and three or four on many of the orbits. Several of the other imaging periods have days without any imaging coverage; for the purposes of time series analysis, brightness values on these missing days were interpolated in time from those for the previous and following days. All of the datasets have occasional data losses over restricted ranges of latitude. These gaps were filled by interpolating across latitude; the results of the time series analyses were almost identical when redone with data interpolated in time instead. Cloud-tracked wind coverage was also extensive enough in spring 1980 and spring 1982 to permit time series analysis of the winds at these times (although time mean wind profiles are available for all five of the primary imaging periods). The basic digital cloud tracking technique used to derive these winds and results for the first imaging period are described in Rossow et al. (1980). An improved version of the tracking method and mean winds and eddy statistics for all five imaging periods are presented in Rossow et al. (1989). Mean zonal wind profiles can also be found in Rossow (1985).

Details of the image processing and Fourier analysis techniques are given in Rossow et al. (1980) and Del Genio and Rossow (1982). Briefly, the images are first navigated and normalized to remove scattering geometry effects on the brightness field, using a scattering model of the main cloud consistent with polarimetry data. Pixels with cosine of either solar or satellite zenith angle < 0.15 are discarded, as are all data poleward of 70° latitude in each hemisphere. The remaining data are sorted to a resolution of 1° latitude and one day and averaged over all longitudes. The resulting evenly spaced time series at each latitude are then Fourier analyzed. Time series of zonal and meridional winds are limited to the latitude range 54°S–46°N and are defined at 4° latitude intervals. The longitudinal averaging implies that the results should be interpreted as time variations of the planetary-scale brightness and wind patterns, primarily zonal wavenumber 1 (Del Genio and Rossow 1982). The one-day sampling interval restricts us to wave periods > 2 days (the Nyquist period). Spectral resolution is inversely proportional to the length of a given image dataset.

The analysis method used here differs slightly from that of Del Genio and Rossow (1982) in several respects. The earlier study used deviations from the disk averaged brightness as the input for the time series analysis. Since the disk average is dominated by low latitude pixels, high latitude spectra are thus contaminated by the effects of equatorial brightness variations. In this paper we use a measure of the absolute normalized brightness (disk average plus deviation), which gives a better representation of local (in latitude) brightness variations. Furthermore, we linearly detrend the time series before computing the spectrum to eliminate spurious power at low frequencies. These changes reduce spectral power away from the locations of the peaks but have no effect at all on the frequency or latitude at which significant peaks occur. (Compare, e.g., Fig. 1, upper left, of this paper with Fig. 2 of Del Genio and Rossow 1982.) Finally, in this paper we present the spectra at each latitude rather than averaging over 20° latitude bands to better define the location of the diagnosed waves.

3. Periodicities in UV brightness

The power spectrum of UV brightness fluctuations for each of the 8 Pioneer Venus imaging datasets is displayed in latitude–frequency space in Figs. 1 and 2. The spectral amplitudes are normalized such that the contours represent constant statistical significance levels. This emphasizes the most prominent signals at the expense of weaker ones. The peaks in these figures thus appear to be somewhat more monochromatic than is actually the case [see Del Genio and Rossow (1982) for comparison]. The precise periods and propagation speeds for each of the significant (at the 95% level or better) spectral peaks are given in Table 2.

The nominal mission data (spring 1979) are dominated by a periodicity of 3.94 ± 0.12 days centered near the equator and extending to about 20° latitude in each hemisphere (Fig. 1, upper left). Composite images constructed from the data demonstrate that this period is the manifestation of the zonal motion of the dark equatorial band associated with the well-known *Y*-feature (Del Genio and Rossow 1982). This result is consistent with both ground-based (Dollfus 1975) and Mariner 10 (Belton et al. 1976) experience. A second spectral peak occurs in midlatitudes of both hemispheres with a period of 5.20 ± 0.22 days. The composite images indicate that this peak is caused by oscillations in the position of the prominent bright polar bands.

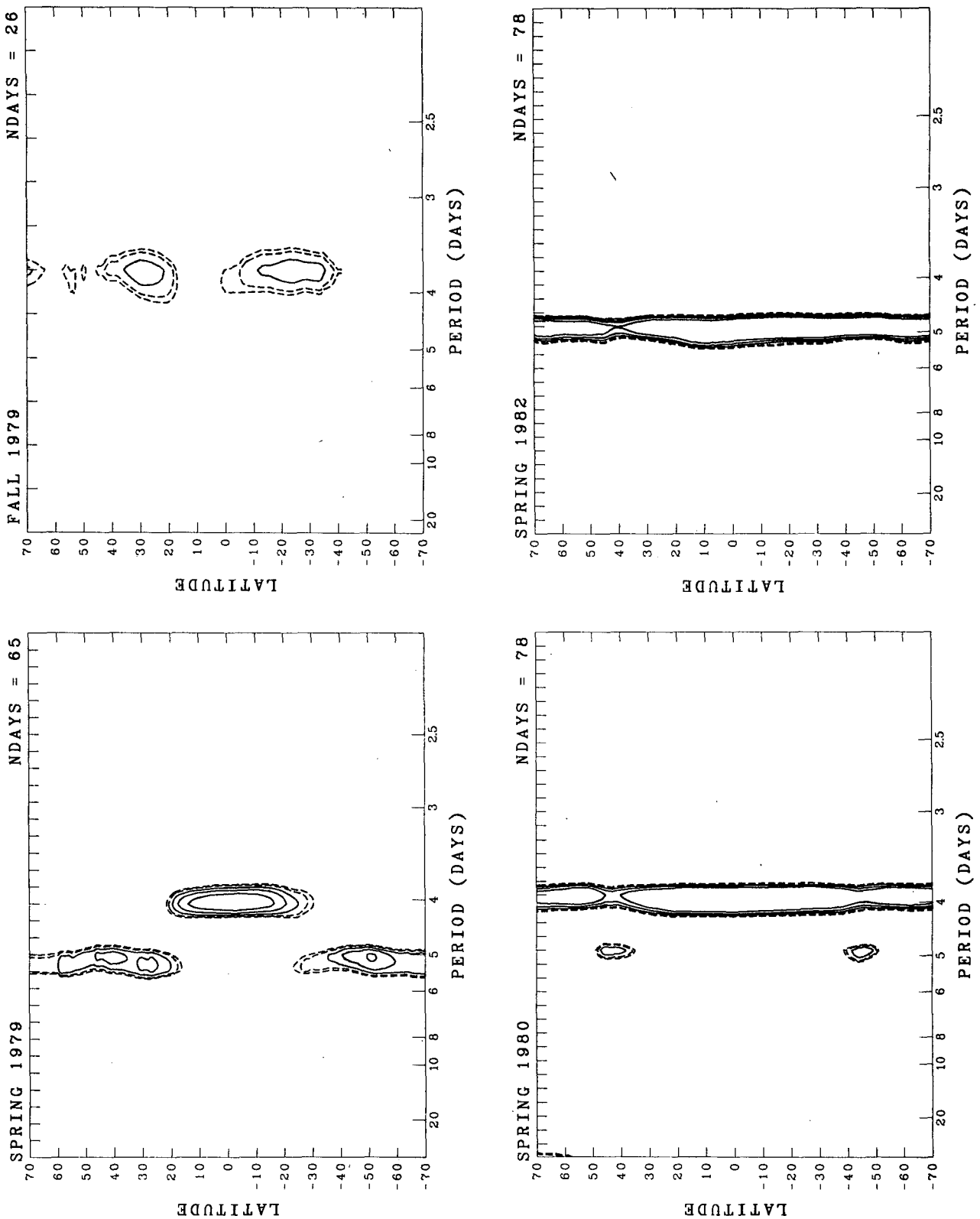

FIG. 1. Time series power spectra of UV brightness fluctuations as a function of latitude and wave period. The contours represent constant statistical significance at the 75% and 85% levels (dashed) and the 95%, 99%, and 99.9% levels (solid) with respect to a white noise spectrum for 2.6 degrees of freedom (Del Genio and Rossow 1982). Tickmarks at top indicate resolved frequencies in cycles/NDAYS. NDAYS is 1 less than the values given in Table 1 because of the Fourier analysis procedure (Rossow et al. 1980). Upper left: spring 1979; upper right: fall 1979; lower left: spring 1980; lower right: spring 1982.

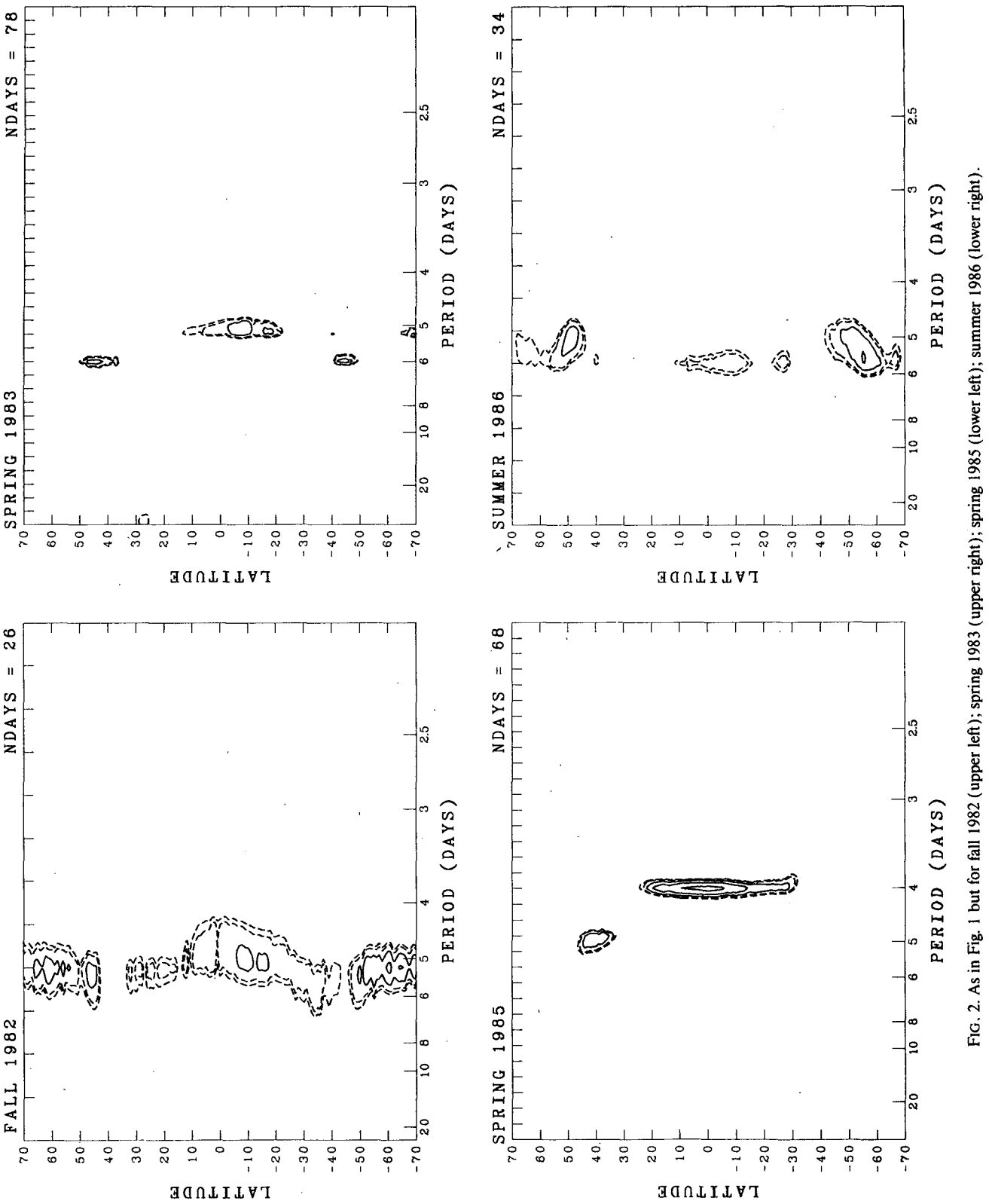

FIG. 2. As in Fig. 1 but for fall 1982 (upper left); spring 1983 (upper right); spring 1985 (lower left); summer 1986 (lower right).

TABLE 2. Propagation characteristics of statistically significant (>95%) transient wave modes in UV brightness time series. Error bars on brightness periodicities are estimated according to the spectral resolution of the time series for each epoch. Only those midlatitude modes with periods distinct from the corresponding equatorial mode are listed.

Epoch	Brightness		Mean zonal wind		$c - \bar{u}$ (m s^{-1})
	Period (d)	c (m s^{-1})	Period (d)	$\bar{u}$ (m s^{-1})	
			Equatorial modes		
Spring 1979	3.94 ± 0.12	111 ± 3	4.66 ± 0.10	95 ± 2	16 ± 5
Fall 1979	4.00 ± 0.33	109 ± 9	—	—	—
Spring 1980	4.00 ± 0.11	109 ± 3	4.73 ± 0.11	94 ± 2	15 ± 5
Spring 1982	5.03 ± 0.17	87 ± 3	5.01 ± 0.12	89 ± 2	−2 ± 5
Fall 1982	4.73 ± 0.47	92 ± 9	—	—	—
Spring 1983	5.03 ± 0.17	87 ± 3	4.96 ± 0.11	90 ± 2	−3 ± 5
Spring 1985	4.00 ± 0.12	109 ± 3	4.59 ± 0.10	97 ± 2	12 ± 5
			Midlatitude modes		
Spring 1979	5.20 ± 0.22	59 ± 2	3.47 ± 0.08	92 ± 2	−32 ± 4
Spring 1980	5.03 ± 0.17	61 ± 2	3.43 ± 0.08	93 ± 2	−32 ± 4
Fall 1982	5.20 ± 0.58	59 ± 6	—	—	—
Spring 1983	6.00 ± 0.24	51 ± 2	3.40 ± 0.08	94 ± 2	−43 ± 4
Spring 1985	5.04 ± 0.19	61 ± 2	3.36 ± 0.08	95 ± 2	−34 ± 4
Summer 1986	5.23 ± 0.44	59 ± 5	—	—	—

Ground-based observers originally interpreted the motion of the Y as the zonal advection of planetary-scale UV markings by a strong retrograde wind at cloud levels, thus giving rise to the idea that the Venus atmosphere superrotates. Young (1975) speculated that the UV features might reflect merely the phase propagation of atmospheric waves instead, with no mass motion. Belton et al. (1976) noted that the motion of the Y in Mariner 10 images appeared to be inconsistent with the cloud-tracked wind speeds derived from displacements of small-scale features. They suggested that the Y might be due to planetary-scale waves propagating at slow speeds relative to a background superrotating wind.

The long temporal coverage of the OCPP images gives us the spectral resolution and sampling necessary to quantitatively resolve differences between the motions of small- and large-scale features. The 3.94-day equatorial period of the large-scale features implies a propagation speed of 111 ± 3 m s^{-1} relative to the solid planet. The mean equatorial cloud-tracked wind speed for spring 1979, by comparison, is 95 ± 2 m s^{-1} (Rossow et al. 1989). This implies that the Y is indeed a planetary-scale wave propagating at a phase speed of 16 ± 5 m s^{-1} prograde with respect to the wind. The spatial uniformity of the 3.94-day period in the presence of a background zonal wind whose angular velocity varies by 15% over ±30° latitude (Rossow et al. 1989) reinforces the notion that the Y is a wave, a point first made by Belton et al. (1976). The midlatitude 5.20-day mode, on the other hand, has a phase speed of 59 ± 2 m s^{-1} compared with the local cloud-tracked wind speed of 92 ± 2 m s^{-1} Thus the oscillations of the polar bands can also be interpreted as waves, these retrograding with respect to the flow at a phase speed of −32 ± 4 m s^{-1}.

The extended mission coverage of Pioneer Venus enables us to monitor the long-term temporal evolution of these wave features. The fall 1979 imaging epoch has coarse spectral resolution because of its short duration, but it shows a low latitude peak at a period of 4.00 ± 0.33 days (Fig. 1, upper right) which is consistent with the spring 1979 observation. The 4-day wave in fall 1979 has its highest amplitude at ±30° latitude, suggesting that the phenomenon is broadening. However, spectral power at the equator is still a maximum at 4 days period. The spring 1980 epoch (Fig. 1, lower left) provides the clearest signature of the wave (period 4.00 ± 0.11 days, relative phase speed 15 ± 5 m s^{-1}), whose influence by this time is global. The spring 1980 data also indicate the presence of a weak midlatitude mode at 5.03 ± 0.17 days period, perhaps related to the 5.20-day mode from spring 1979.

Between 1980 and 1982 there was apparently a transition in the dynamical state of the cloud level atmosphere. The equatorial cloud-tracked wind speed decreased to 89 ± 2 m s^{-1} (Rossow et al. 1989). Coincident with this the large-scale UV brightness distribution shifted from the approximate 4-day periodicity characteristic of earlier epochs to a 5.03 ± 0.17 day periodicity (Fig. 1, lower right), implying an equatorial propagation speed of 87 ± 3 m s^{-1}. The wind-relative propagation speed of −2 ± 5 m s^{-1} at the equator is not significantly different from zero, although it becomes so at higher latitudes. Three possibilities therefore exist: 1) A different, very slowly moving equatorial wave is present at this time; 2) Midlatitude retrograding waves are controlling the global brightness;

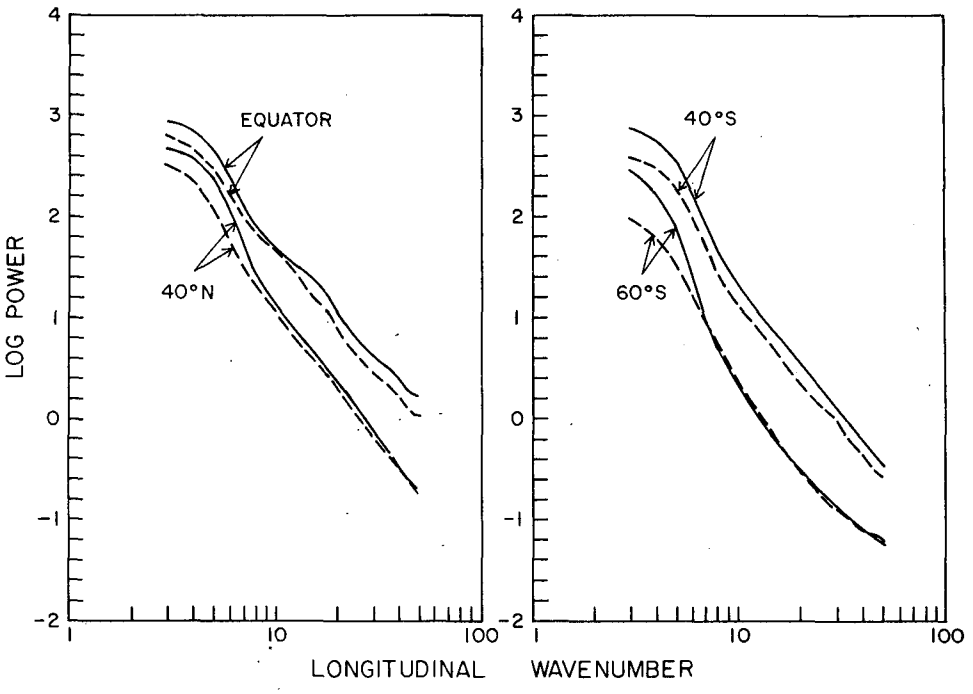

FIG. 3. Mean longitudinal power spectra of UV brightness fluctuations at various latitudes for the spring 1980 (solid) and spring 1982 (dashed) epochs.

and 3) The observed brightness patterns reflect the pure advection of remnant UV markings without any active wave propagation. The second possibility is unlikely, because variance in midlatitude brightness was lower in spring 1982 than at any other time in the history of OCPP imaging, especially at low wavenumbers (Fig. 3). Furthermore, we show in section 4 that wind spectra for this epoch indicate no organized midlatitude wave activity even at the 75% confidence level (Fig. 8). It is difficult to distinguish the other two possibilities with brightness information alone, although the equatorial brightness variance was also slightly diminished in spring 1982. In any case, it is certain that the canonical 4-day wave is undetectable in UV brightness data in spring 1982. A similar situation exists in the short fall 1982 dataset (Fig. 2, upper left), the diagnosed equatorial period being 4.73 ± 0.47 days.

The spring 1983 spectrum (Fig. 2, upper right) has similar characteristics at low latitudes (period 5.03 ± 0.17 days, wind-relative phase speed -3 ± 5 m s^{-1}), but the amplitude of the spectral peak is much smaller than that present in spring 1982. This is consistent with the idea that the spring 1982 feature is a remnant of a previous wave mode, since we would expect the features to decay in the absence of the wave-induced perturbations that create the UV contrasts. There is some evidence to suggest that fall 1982–spring 1983 is a time of transition between dynamical states: the appearance of a long-period midlatitude mode in both datasets (5.20 ± 0.58 days in the former, 6.00 ± 0.24 days in the latter), and a long-term trend in the disk-averaged brightness in spring 1983, which is absent from the other imaging epochs. The brightness spectrum in 1983 also shows the return of a weak, statistically insignificant 4-day peak; the 4-day signal is more obvious at this time in the zonal wind record (Rossow et al. 1989). This raises the possibility that the response of the UV albedo field as a tracer for the large-scale dynamics is lagged.

By spring 1985 the Venus atmosphere has returned to a configuration much like that of spring 1979 (Fig. 2, lower left), with a distinct periodicity of 4.00 ± 0.12 days confined to latitudes equatorward of about 20° and a midlatitude mode of period 5.04 ± 0.19 days. (Peaks occur at this period in both the Northern and Southern hemispheres, but only the northern feature is statistically significant because of frequent data gaps in the other hemisphere in this epoch.) A short dataset obtained in summer 1986 (Fig. 2, lower right) shows similar behavior in midlatitudes; at the equator this epoch exhibits a double peak at 5.67 days (85% confidence) and 3.58 days (<75% confidence), neither of which is significant. Cloud-tracked winds for spring 1985 have also returned to nominal mission levels (97 ± 2 m s^{-1} at the equator), implying a prograde phase speed there of 12 ± 5 m s^{-1}.

If the features we see are truly planetary-scale waves, their oscillations should be coherent and in phase over broad ranges of latitude. Figure 4 shows the coherence squared and phase difference in spring 1979 for the 4-

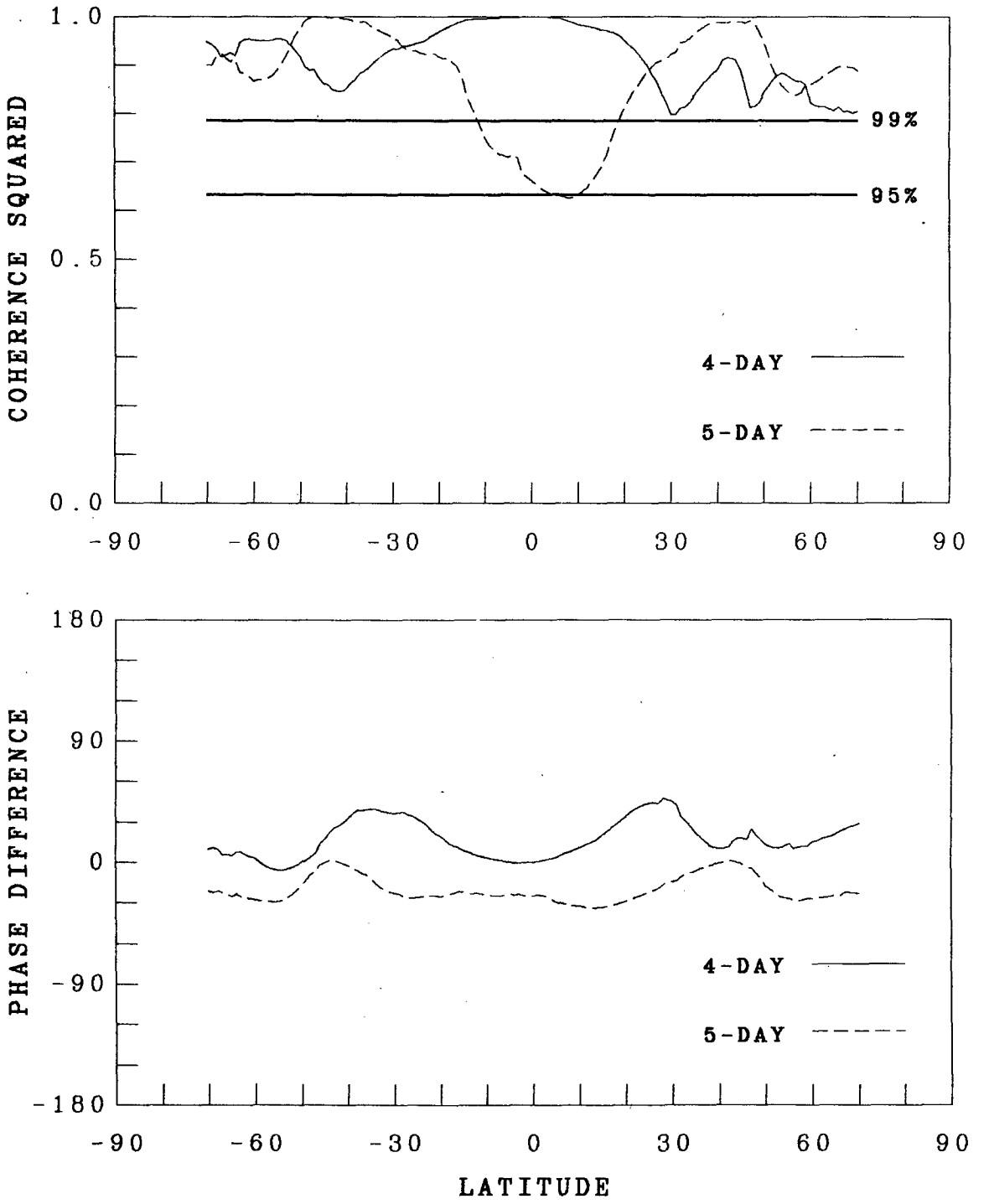

FIG. 4. Latitudinal profiles of coherence squared (upper) and phase difference (lower) of the 4-day wave with respect to the equator (solid) and the 5-day wave with respect to 45°S (dashed) for the spring 1979 epoch. The heavy solid lines are 95% and 99% confidence levels for 4 degrees of freedom.

day wave with respect to the equator, and for the 5-day wave with respect to 45°S latitude. To calculate coherence, we replace sums over independent realizations of the spectrum with sums over four adjacent frequency bands (Thompson 1979), the maximum possible with our coarse spectral resolution. The Hanning procedure we apply to the time series (Rossow et al. 1980) implies that this is equivalent to 5 degrees of

freedom. However, we compute significance assuming a more conservative 4 degrees of freedom.

Figure 4 demonstrates that the 4-day oscillation at the equator is coherent over the entire planet, supporting the notion that it is indeed a planetary-scale wave. Oscillations at ±30° latitude lead that at the equator by almost 45° in phase, a signature of the tilt in the arms of the *Y*. The high coherence at these latitudes suggests that the process that creates the arms of the *Y* is tied to the wave responsible for the dark equatorial band. The 5-day oscillation in southern midlatitudes is highly coherent and in phase with that in northern midlatitudes, but only marginally coherent with equatorial oscillations. Thus, the 5-day signal appears to represent a symmetric midlatitude wave mode. The high coherence at 5 days down to ±30° latitude and an accompanying 30° phase shift might be evidence of an interaction between the 4- and 5-day waves (Belton et al. 1976; Del Genio and Rossow 1982).

The temporal evolution of the coherence is illustrated in Fig. 5. The 4-day wave is even more globally coherent in spring 1980, but by spring 1982, coherence drops off rapidly away from the equator, further proof that the 4-day wave has virtually disappeared. Coherence increases somewhat in 1983 and 1985, as the 4-day wave returns, but the impression is that the wave in 1985 is not yet as dominant as it had been in 1979. The 5-day wave has a phase (not shown) and coherence pattern in 1980 and 1983 qualitatively similar to that in 1979. The relatively low coherence in 1985 may either be a result of large data losses in midlatitudes or a real indication of asymmetry due, for example, to a midlatitude instability. The clear exception is spring 1982, the only time at which the 5-day signal is coherent and in phase globally. Since transient wave activity is at a minimum in both brightness and winds (see section 4) in spring 1982, this behavior must be due to advection of existing markings. However, it is unclear how the features remain globally coherent in the face of the Doppler shift caused by latitudinal shear of the zonal wind.

Taken together, the entire history of Pioneer Venus OCPP image observations suggests that the cloud level atmosphere vacillates between two distinct dynamical states on a time scale of perhaps 5–10 years (Fig. 6). In one configuration, planetary-scale equatorial waves and associated slowly moving midlatitude wave modes are active, and equatorial zonal winds are a maximum. Over a 2–3 year interval this gives way to an alternate configuration in which equatorial waves are weaker, absent or different in character and equatorial zonal winds are weaker. Shorter time scales are ruled out by the temporal resolution of our imaging epochs (Table 1, Fig. 6), but longer time scales are possible. Our impression of cyclic variation is tentative, since the Pioneer Venus record spans only one such "cycle." The interpretation is plausible, though, because similar behavior occurs in the Earth's stratosphere; we compare the Venus and Earth cases in section 6.

4. Relationship of UV markings to wind fluctuations

The results of the preceding section lead naturally to the speculation that changes in the generation or propagation of equatorial planetary-scale waves are not only correlated with but causally related to variations in the cloud level wind speed. If true this would identify a significant contributor to the cloud level momentum balance. To make this connection it is necessary to identify the specific wave modes that give rise to the markings and to estimate the direction and magnitude of the associated eddy momentum flux.

Unfortunately, the UV features by themselves cannot be interpreted in terms of useful meteorological variables. However, if the markings do indicate waves, then correlated fluctuations in wind, temperature, and pressure on similar time and space scales should accompany them. If uncertainties in daily cloud-tracked wind values are not too large compared to wave amplitudes, we can Fourier analyze time series of longitudinal mean zonal and meridional wind fluctuations in the same manner used to document UV brightness fluctuations. The spring 1980 and spring 1982 cloud-tracked winds are sufficiently extensive and continuous in time to permit such analysis.

Figure 7 shows the power spectrum of zonal (u') and meridional (v') wind perturbations for the spring 1980 epoch. Low-latitude zonal wind fluctuations exhibit a spectral peak at a period of 3.90 ± 0.10 days at the 95% confidence level, consistent with the brightness spectral peak observed at this time (Fig. 1, lower left). The amplitude of this oscillation $u' \approx 4$–5 m s^{-1}. This confirms our hypothesis that the UV markings are tracers of planetary-scale atmospheric wave motions. An additional equatorial peak in u' occurs at 4.88 ± 0.15 days; we will discuss this later. In contrast, time series analysis of the spring 1982 cloud-tracked winds yielded no statistically significant periodicities, although a weak (≤ 1 m s^{-1} amplitude) 4-day remnant is suggested in zonal wind composites (Rossow et al. 1989). In fact, the zonal wind spectrum for spring 1982 does not even have a local maximum in equatorial power at the 5-day brightness period and only exhibits a weak (85% confidence) 5-day peak in southern midlatitudes (Fig. 8). Given the absence of coherent wind oscillations to support the production of UV contrasts, we conclude that the 1982–83 epochs reflect a quiescent state of the cloud-level equatorial atmosphere. The UV patterns during these two years must then be regarded as decaying remnants of earlier wave activity, being advected around the planet while dissipating due to horizontal mixing. We will estimate the strength of this mixing at the end of this section.

Identification of the 4-day wave is more uncertain than similar determinations of equatorial wave types in the Earth's stratosphere (cf. Wallace and Kousky 1968), because we do not have correlative temperature data or information on vertical phase variations. We can, however, constrain the possibilities by comparing

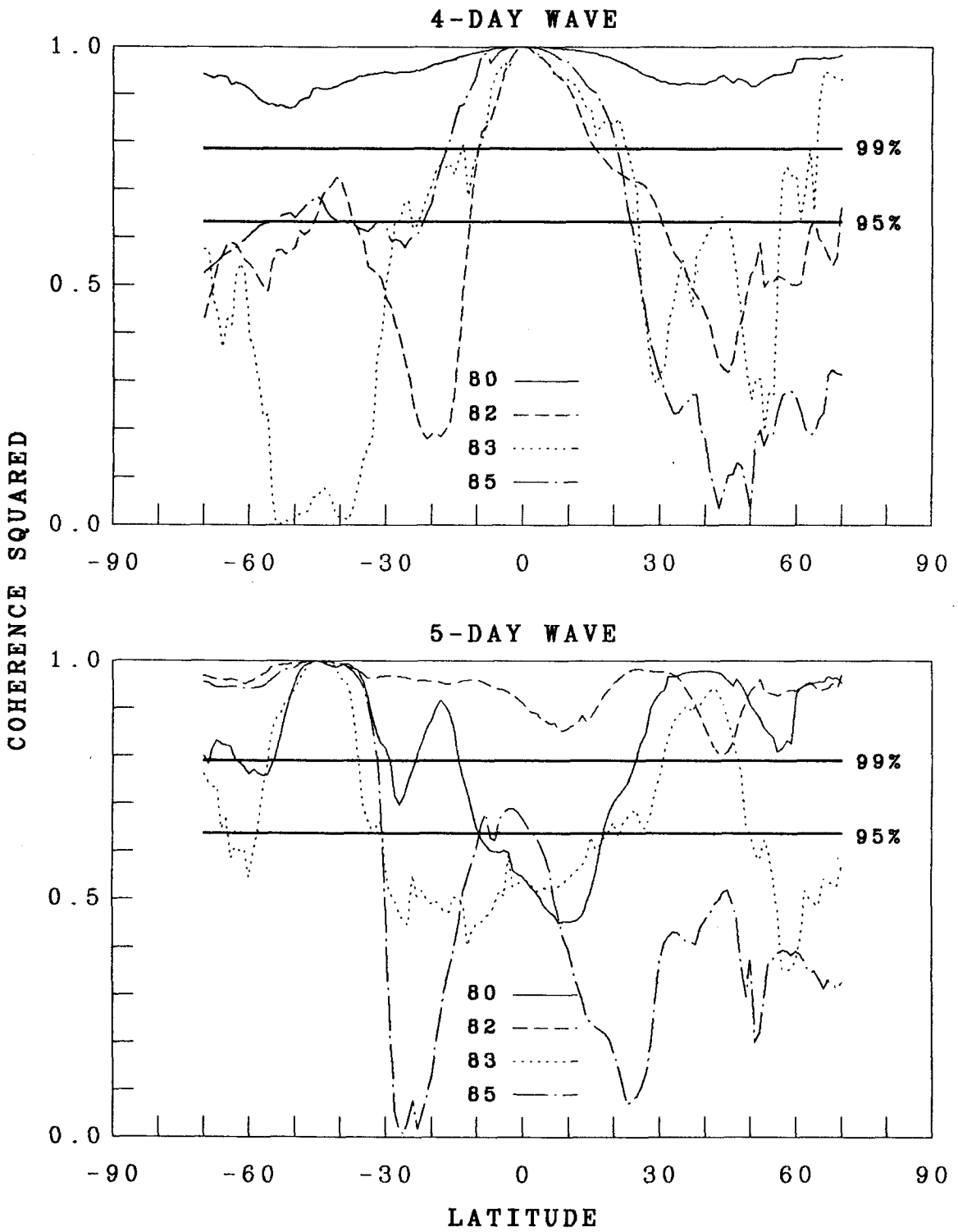

FIG. 5. Latitudinal profiles of coherence squared for the 4-day (upper) and 5-day (lower) waves (as in Fig. 4) for the spring 1980 (solid), spring 1982 (dashed), spring 1983 (dotted), and spring 1985 (dash–dot) epochs.

the diagnosed propagation characteristics and spatial extent of the wave with the predictions of classical atmospheric wave theory (Longuet-Higgins 1968). The prograde propagation speed of the wave with respect to the mean wind (i.e., in the direction of planetary rotation) immediately rules out all Rossby modes as well as the mixed Rossby–gravity (Yanai) mode. Antisymmetric inertia–gravity modes, which reflect

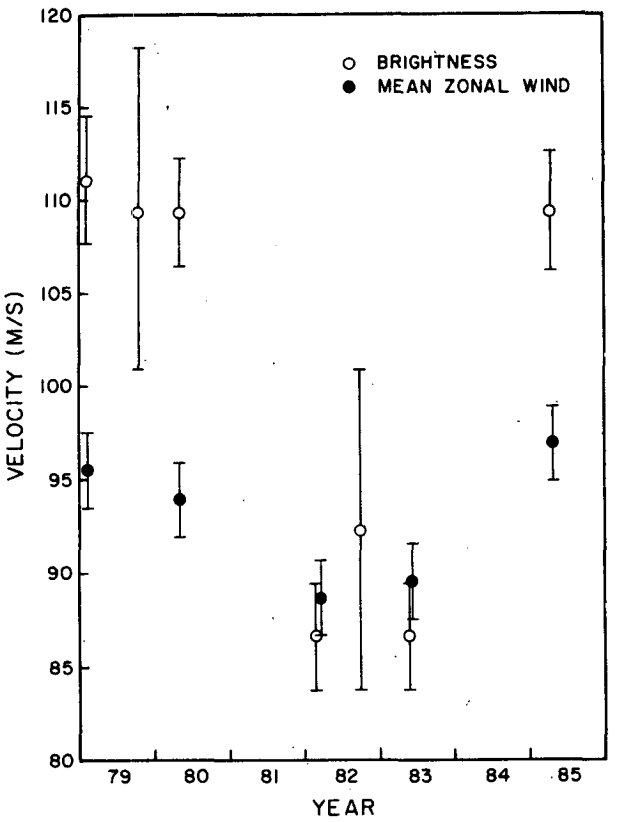

FIG. 6. Mean equatorial cloud-tracked zonal wind speeds (filled circles) and propagation phase speeds implied by large-scale equatorial UV brightness periodicities (open circles) for all available epochs. Wind error bars are taken from Rossow et al. (1989). Brightness error bars are determined by the frequency resolution of the power spectrum for each epoch.

asymmetric forcing, are inconsistent with the apparent hemispheric symmetry of the observed waves (Figs. 4, 5). The symmetric inertia–gravity waves have maximum u' off the equator; this mode may contribute in epochs such as fall 1979 and spring 1980 but cannot explain the general tendency for an equatorial maximum.

The only remaining mode, the Kelvin wave, has properties that are consistent with all the available information from Pioneer Venus. The Kelvin wave propagates in the direction of planetary rotation and peaks in amplitude at the equator. On an equatorial β-plane in the absence of shear, linear wave theory predicts that the decay of amplitude with latitude is Gaussian with an e-folding distance

$$\theta_{e\text{-fold}} = \frac{360^\circ}{2\pi a}\left|\frac{(c-\bar{u})a}{\Omega}\right|^{1/2}, \qquad (1)$$

where a is the planetary radius, c the phase speed, $\bar{u}$ the mean zonal wind speed, and Ω the planetary rotation rate. For our purposes, the relevant Ω is probably that defined by a coordinate system rotating with the mean wind at cloud level. Thus, with $\Omega = 2\pi(4.66\text{ d})^{-1}$, $a = 6115$ km, and $c - \bar{u} = 16$ m s^{-1}, we get $\theta_{e\text{-fold}} = 23^\circ$. This is comparable to the latitudinal extent of both the dark equatorial band in the UV images and the statistically significant brightness fluctuations for the spring 1979 and spring 1985 epochs (Figs. 1, 2).

The Kelvin wave is essentially a two-dimensional gravity wave, with oscillations in the longitudinal and vertical directions and zero meridional wind fluctuation at the equator (Longuet-Higgins 1968). The 4-day wave in the OCPP images exhibits such behavior (Fig. 7); there is no spectral peak at low latitudes in time series of v', despite the obvious 4-day period of u'. (See also Rossow et al. 1989.) Inertia–gravity waves, on the other hand, have maxima in v' at low latitudes for the parameter setting appropriate to the Venus 4-day wave. The evidence is thus quite compelling that the equatorial component of the Y-feature is the manifestation of a Kelvin wave at cloud level, as originally suggested by Belton et al. (1976).

The vertical structure of planetary-scale waves in a stratified atmosphere depends on the eigenvalue of Laplace's tidal equation $\epsilon = 4\Omega^2 a^2/gh$, where h is called the equivalent depth (the depth of a homogeneous, incompressible fluid whose oscillations would be equivalent to those present in the stratified compressible atmosphere). In the absence of shear, the vertical wavelength is given by

$$\lambda_z = 2\pi\left(\frac{N^2}{gh} - \frac{1}{4H^2}\right)^{-1/2} \qquad (2)$$

where N is the Brunt–Väisälä frequency, H the scale height, and g the acceleration due to gravity. For Kelvin waves $(gh)^{1/2} = c - \bar{u}$, implying that $h = 0.03$ km. The effects of vertical wind shear on gravity waves can potentially alter (2) so that λ_z becomes imaginary, i.e., the waves are evanescent and do not propagate vertically. Gossard and Hooke (1975) show that wind curvature is generally more important to gravity waves than the shear itself. Taking $N = 1.6 \times 10^{-2}$ s^{-1} at cloud level, we estimate from their dispersion relation with curvature that the Kelvin wave will propagate vertically if

$$\left|\frac{d^2\bar{u}}{dz^2}\right| < \frac{N^2}{|\bar{u}-c|} \approx 16 \text{ m s}^{-1}\text{ km}^{-2}, \qquad (3)$$

which is satisfied by an order of magnitude in the Pioneer probe and radio occultation wind profiles (Counselman et al. 1980; Newman et al. 1984). Thus, the wave clearly propagates vertically without confinement. With $H = 5.2$ km, the vertical wavelength can then be estimated from (2) to be $\lambda_z \approx 6$ km.

Chang (1977) has shown that viscous and thermal damping can increase the vertical wavelength of Kelvin waves. At cloud top, data on turbulence levels and the vertical profiles of various constituents suggest that the eddy diffusivity $\kappa_v \approx 2$ m^2 s^{-1} (von Zahn et al. 1983), implying a momentum damping time scale $\tau_m \approx 15$–20 days for perturbations with vertical wavelengths

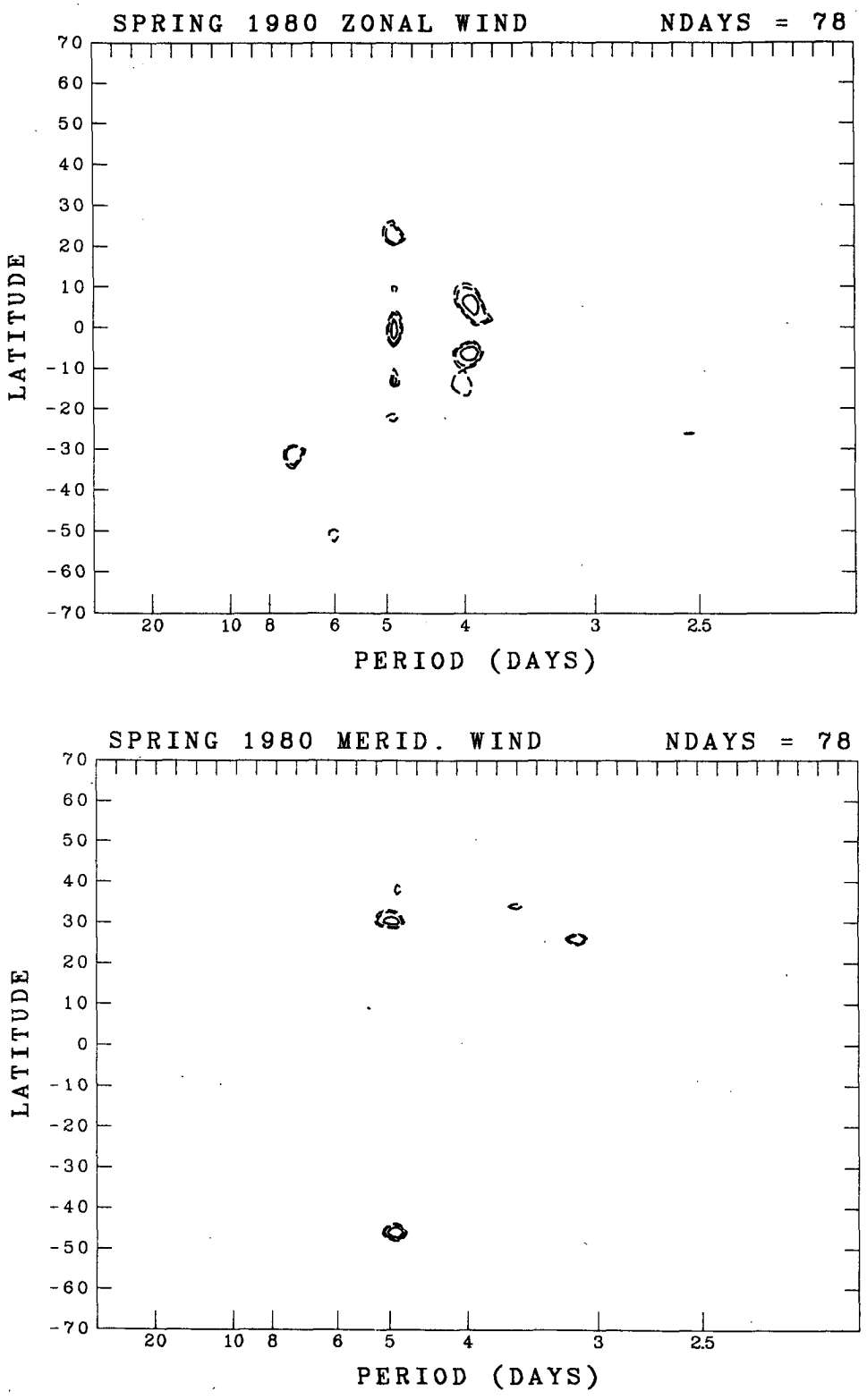

FIG. 7. Time series power spectra of cloud-tracked zonal (upper) and meridional (lower) cloud-tracked wind fluctuations for the spring 1980 epoch. Contours as in Fig. 1.

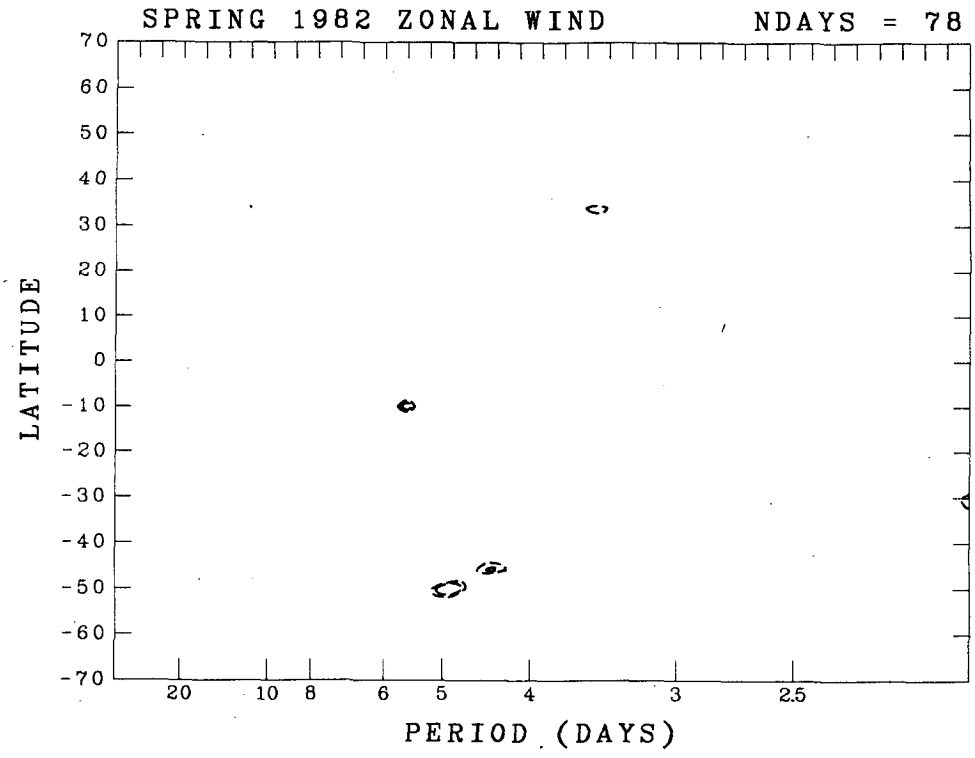

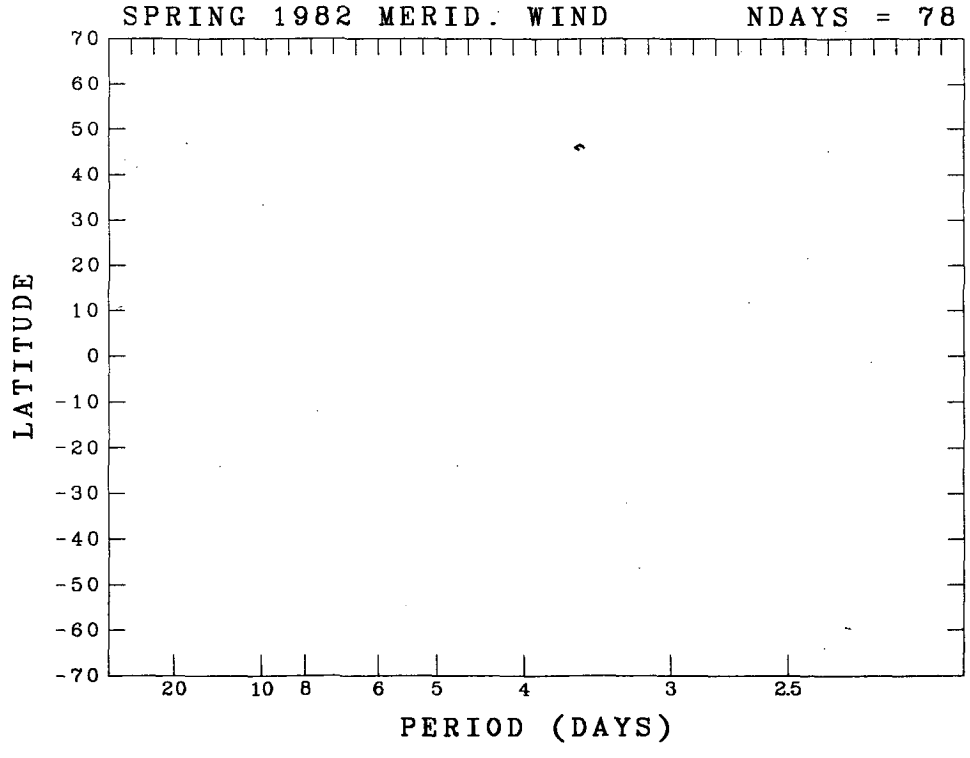

FIG. 8. As in Fig. 7, but for spring 1982.

somewhat in excess of 6 km. Radiative damping is more important; we estimate its time scale as $\tau_r \approx 4$ days for such perturbations (Crisp 1989). This gives $\lambda_z \approx 11$ km instead, using Chang's formalism corrected for unequal momentum and thermal damping. The UV absorber must therefore produce an effective OCPP weighting function no broader than about $\lambda_z/2$, i.e., a scale height or less, or else it would not be possible to see the *Y*-feature in the images. This is consistent with our earlier estimate that the UV markings originate within the 65–70 km altitude range. OIR weighting functions, however, are comparable to λ_z, and it is therefore not surprising that the 4-day oscillation is not observed in the infrared. Pechmann (1983) has discussed the same effect in relation to the diurnal thermal tide. Radio occultation temperature soundings with fine vertical resolution at the equator, on the other hand, sometimes exhibit oscillatory structure above 100 mb with a vertical scale near λ_z (Kliore and Patel 1980, Fig. 9).

The above estimates neglect the effects of latitudinal wind shear on wave structure. Boyd (1978) has examined the effects of meridional shear on equatorial waves in the limit of small λ_z relative to the vertical scale of mean zonal wind variations, a condition easily satisfied for the Venus Kelvin wave. His results indicate that Kelvin waves of planetary scale are extremely insensitive to even strong latitudinal shear. Applying Boyd's formulas to the weak low-latitude shear implied by the cloud-tracked winds (Rossow et al. 1989), we estimate that shear effects on $\theta_{e\text{-fold}}$, λ_z, and u' are at best a few percent for a Venus Kelvin wave with horizontal wavelength $\lambda_x = 2\pi a$. Linear shear does induce a nonzero v' at the equator, but its magnitude is <1 m s^{-1}, smaller than the uncertainty in the cloud-tracked winds.

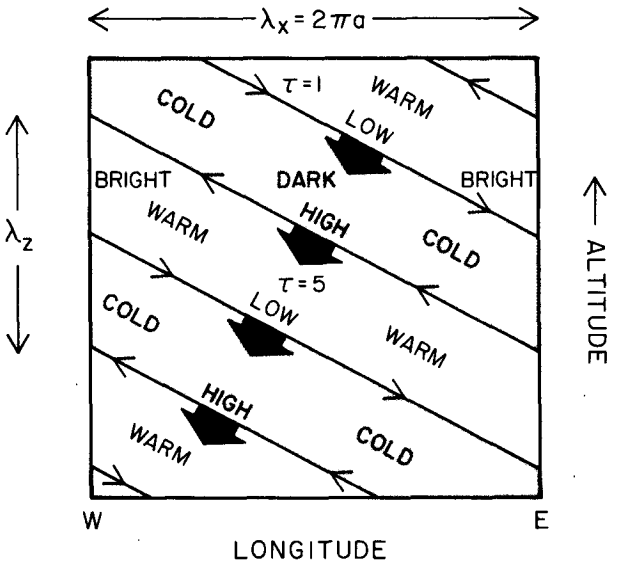

FIG. 9. Schematic diagram illustrating the structure of the Kelvin wave perturbation in the longitude-altitude plane and its relationship to the UV markings in the absence of damping. The thin arrows indicate the direction of zonal and vertical displacements by the wave; the heavy arrows denote the direction of phase propagation. The sense of temperature and pressure perturbations is also indicated.

The implied structure of the Kelvin wave in the absence of phase lags produced by damping is indicated schematically in Fig. 9. Zonal and vertical wind perturbations are roughly in phase, so momentum of the same sign as the superrotation is transported upward. Energy is also transported upward, while phase propagates downward. Dark UV features are produced by upwelling of absorber concentrated below cloud top over a half cycle of the wave, and bright features by downwelling over the other half cycle. In the presence of small-scale vertical diffusion, the perturbation concentration of absorber n' is related to the vertical velocity perturbation w' and the mean absorber concentration $\bar{n}$ by

$$\frac{\partial n'}{\partial t} + w' \frac{d\bar{n}}{dz} = \kappa_v \frac{\partial^2 n'}{\partial z^2}. \tag{4}$$

For waves with frequency ω and vertical wavenumber $\mu \gg (2H)^{-1}$,

$$n' \approx -\frac{d\bar{n}}{dz} \frac{\kappa_v \mu^2 + i\omega}{\kappa_v^2 \mu^4 + \omega^2} w'$$

$$= w'C \exp\left(i \tan^{-1} \frac{\omega}{\kappa_v \mu^2}\right) = w'C \exp(i\phi), \tag{5}$$

where the constant $C > 0$ because the UV absorber is embedded below cloud top ($d\bar{n}/dz < 0$). Thus, dark regions should lag maximum upwelling (and maximum zonal winds) by $0° < \phi < 90°$ depending on the strength of diffusion. We can test this assertion by cross-correlating our time series of brightness and cloud-tracked zonal winds. The result for the spring 1980 epoch, during which the 4-day wave was active, is shown in Fig. 10. Statistically significant positive (negative) correlations exist for lags of 0 and 1 (2 and 3) days over a range of latitudes comparable to the computed *e*-folding width of the Kelvin wave, implying that zonal wind maxima lead dark features by $0° < \phi < 90°$. This is consistent with the simple relationships indicated in Fig. 9. From (5) we estimate $\phi = \tan^{-1}(\omega/\kappa_v\mu^2) = \tan^{-1}[(c - \bar{u})\lambda_z^2/4\pi^2 a\kappa_v] \approx 75°$. The correlations have the same sense in 1979 and 1985 but are less significant due to the sparser wind coverage in these epochs. A similar tendency has also been noted in the short Mariner 10 dataset (Limaye and Suomi 1981). In spring 1982, on the other hand, brightness and wind are largely uncorrelated, and the correlation is independent of lag (Fig. 11); the same is true in spring 1983. This is further proof of the absence of transient planetary-scale wave activity at this time.

The vertical velocity perturbation associated with the wave is related to the zonal wind perturbation by

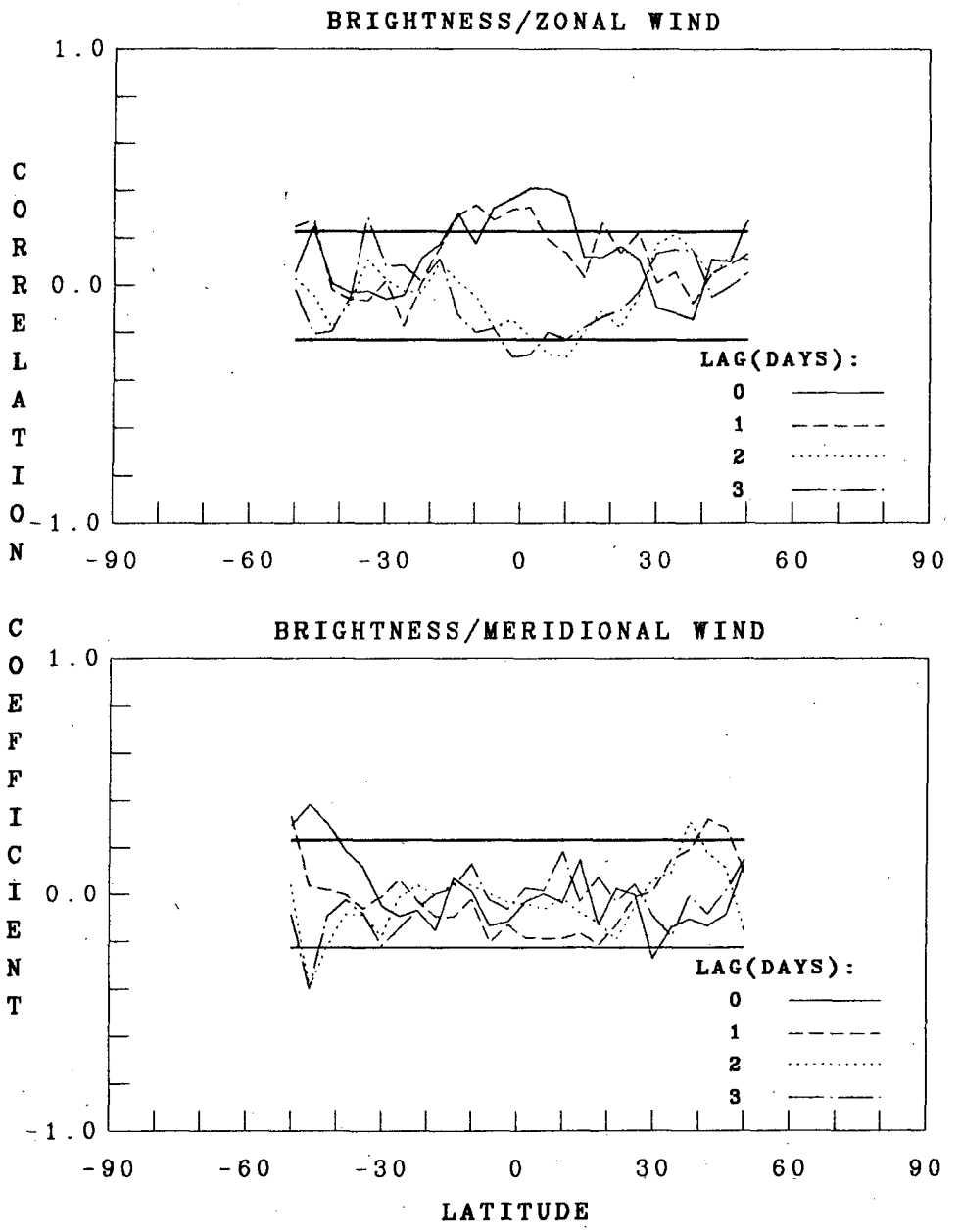

FIG. 10. The correlation coefficients of daily mean time series of UV brightness and zonal (upper) or meridional (lower) wind velocity for various lags as a function of latitude for the spring 1980 epoch. Statistical significance at the 95% level is indicated by the heavy solid lines.

$w' \approx -u'k/\mu$, where $k = 2\pi/\lambda_x$ and $\mu = -2\pi/\lambda_z$ ($\mu < 0$ implies upward energy propagation). We can estimate the temperature perturbation T' from this relation and the thermodynamic energy equation. For radiative damping represented as Newtonian cooling,

$$\frac{\partial T'}{\partial t} + w' \frac{N^2 \bar{T}}{g} = -\frac{T'}{\tau_r}. \tag{6}$$

where $\bar{T}$ is the mean temperature. For waves of frequency ω,

$$T' = -w' \frac{N^2 \bar{T}}{g} (\tau_r^{-2} + \omega^2)^{-1/2} \exp(i \tan^{-1} \omega \tau_r). \tag{7}$$

Taking $\bar{T} = 240$ K, $g = 8.9$ m s^{-2}, $u' = 4.5$ m s^{-1} from the cloud-tracked wind time series analysis, and $\tau_r = 4$ days from Crisp (1989), (7) implies that the magnitude of $T' \approx 2.3$ K, too small to be seen by infrared sensors with broad weighting functions but comparable to the amplitude of weak oscillations seen in the occultation profiles. The temperature perturbation may be large enough to stimulate convection locally; turbulent con-

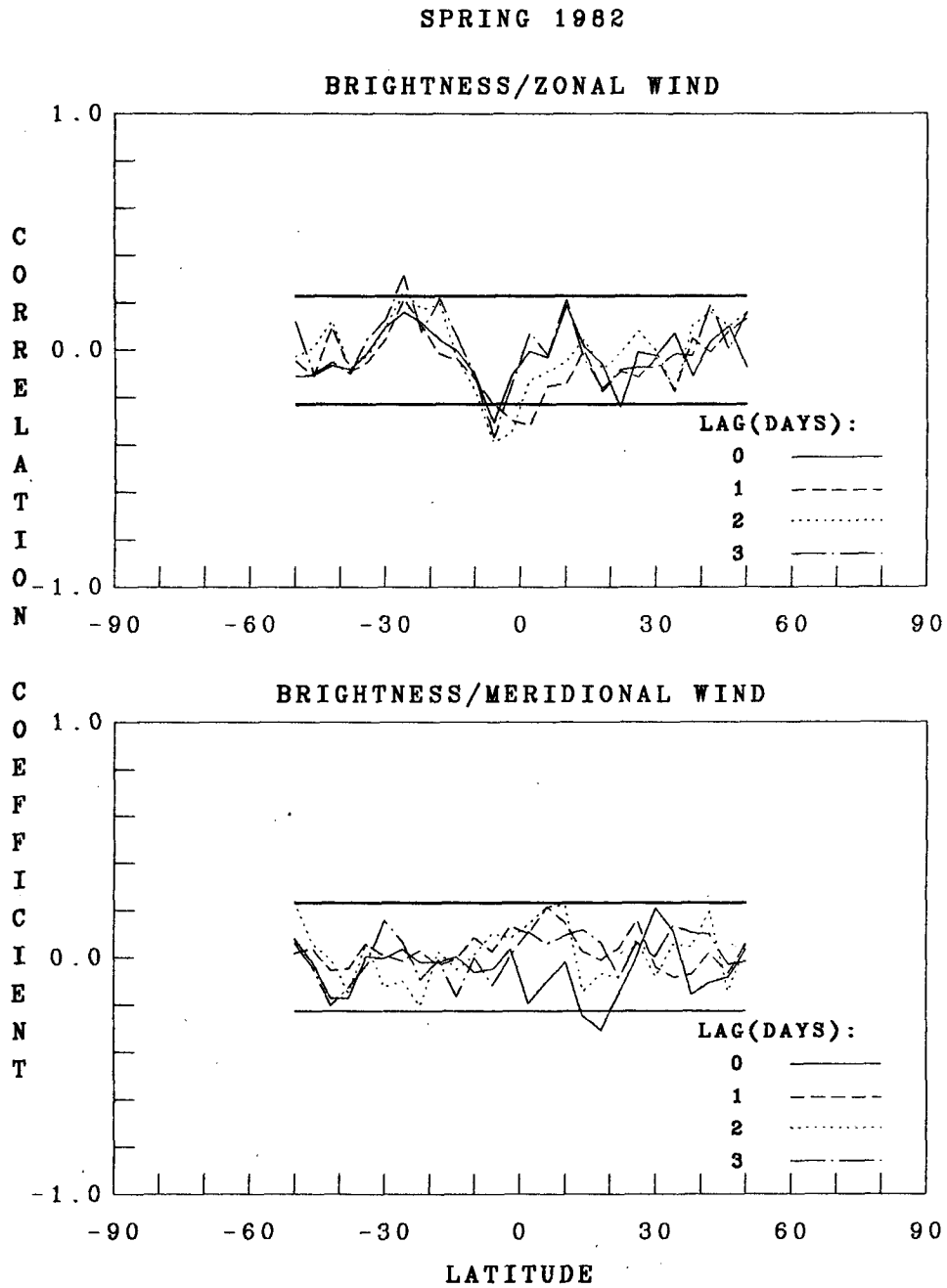

FIG. 11. As in Fig. 10 but for spring 1982.

vective mixing of UV absorber up to the cloud tops might then also contribute to the production of the UV markings. We will return to this point in section 6.

With these results in hand, it is now possible to relate the large-scale UV features at low latitudes to standard meteorological quantities. Specifically, zonal winds peak at the leading edge of the equatorial band (the vertex of the *Y*-feature). Dark regions produced by upwelling lag $< 90°$ behind. Adiabatic cooling (warming) by wave upward (downward) displacements causes negative (positive) temperature anomalies. Since $\tan^{-1}\omega\tau_r \approx 40°$, cold regions lag maximum zonal winds by less than a quarter cycle and should correlate fairly well with dark regions if τ_m and τ_r are not too different.

The vertical velocity perturbation, integrated over one half-cycle of the wave, implies a total vertical displacement of about 1 km. Esposito and Travis (1982) found a correlation between OCPP polarization degree

and UV brightness that suggests a 1 km lowering of the cloud top above dark features. Figure 9 illustrates how this result can be reconciled with our findings. If the $\tau = 1$ level is a distance of about $\lambda_z/2$ above the UV feature level, then sinking motion over a half cycle of the wave at cloud top correlates with upwelling over the other half cycle at the UV feature level. Since $\tau = 1$ is near 70 km, the large-scale low-latitude UV features must then be centered near 65–66 km, which is consistent with our original estimate of their location. We also note that observed 4-day oscillations of CO_2 absorption imply cloud height variations of order 0.5–1.0 km (Young et al. 1974; Crisp and Young 1978).

Identification of the 5-day period midlatitude wave seen in the brightness time series for certain epochs (e.g., spring 1979, 1980, 1985) is greatly facilitated by the spectral analysis of cloud-tracked winds (Fig. 7). Meridional wind fluctuations exhibit a statistically significant peak at a period of 4.88 ±0.15 days in midlatitudes of both hemispheres. There is no corresponding peak in the zonal wind at these latitudes, but there is one at the equator. We estimate $v' \approx 5$–8 m s^{-1} from the midlatitude spectrum and the observed oscillatory displacement of the bright polar bands between 45° and 55° latitude (Del Genio and Rossow 1982). Spectral and coherence analysis (Figs. 1, 2, 4, 5) shows the wave to be roughly hemispherically symmetric, with a retrograde Doppler-shifted phase speed $c - \bar{u} \approx -32$ m s^{-1}.

Retrograde propagation is consistent with either an inertia–gravity or Rossby–Haurwitz mode. Planetary-scale inertia–gravity waves have phase speeds much higher than that observed and similar latitudinal structure in u' and v' (Longuet-Higgins 1968). Rossby–Haurwitz waves, on the other hand, have moderate phase speeds and different u' and v' dependence on latitude for appropriate parameter settings. The meridional structure of an internal Rossby–Haurwitz mode depends on its equivalent depth. We can estimate h from the dispersion relation for a zonally propagating Rossby wave on a midlatitude β-plane. The Doppler-shifted phase speed is given by

$$c - \bar{u} = -\frac{\beta}{k^2 + f_0^2/gh}, \qquad (8)$$

where $f_0 = 2\Omega \sin\theta_0$ is the Coriolis parameter at latitude θ_0 and $\beta = 2\Omega \cos\theta_0/a$ its gradient. Taking $c - \bar{u} = -32$ m s^{-1}, $\Omega = 2\pi(3.47\text{ d})^{-1}$ for a coordinate system rotating with the local wind at $\theta_0 = 45°$, and $k = (a\cos\theta_0)^{-1}$, we obtain $h \approx 1$ km ($\epsilon \approx 10$). For this ϵ, the meridional wind perturbation of the gravest symmetric Rossby mode peaks in amplitude at 45°, consistent with the location of the observed 5-day wave in the brightness and v' spectra. (See also Rossow et al. 1989.) The zonal velocity perturbation for this mode has a node in midlatitudes and a maximum at the equator, precisely the behavior seen in the spectrum of u' (Fig. 7). Marginally significant brightness-meridional wind correlations occur in midlatitudes in spring 1980 (Fig. 10). The sense of these correlations is generally opposite in the two hemispheres, implying a symmetric wave mode. The correlations imply darkening accompanying poleward motion, i.e., displacement of the bright polar bands to higher latitudes.

The vertical wavelength of these waves can also be estimated from (2). Taking $N = 2 \times 10^{-2}$ s^{-1} and $H = 5$ km as characteristic of midlatitudes we obtain $\lambda_z \approx 34$ km. In the presence of meridional shear, the effective planetary vorticity gradient β in (8) should be replaced by the absolute vorticity gradient Z_y (Thompson 1948). In midlatitudes, we crudely estimate $Z_y \approx 10^{-11}$ m^{-1} s^{-1} from cloud-tracked winds. This gives $h = 0.4$ km and $\lambda_z \approx 19$ km instead. Damping may increase λ_z, but we expect its effect to be less than that for the Kelvin wave because the larger λ_z of the Rossby wave implies longer damping time constants. In any case, if the 5-day midlatitude oscillation is a Rossby wave, it propagates vertically but with a much longer wavelength than the equatorial Kelvin wave. If this is so, we might expect to see evidence of the Rossby mode in the OIR data, which have good coverage of high latitudes. Taylor et al. (1980) and Apt and Leung (1982) report a 5.3 day periodicity in midlatitude brightness temperatures in all their sounding channels in 1979. The phase of this oscillation varies by almost 360° between cloud top and 90 km, implying that it freely propagates vertically with an upper limit of 25–30 km for its vertical wavelength, which is consistent with our estimate. It is therefore plausible to identify the 5-day midlatitude mode as the slow rotation equivalent of an internal Rossby–Haurwitz wave.

We note finally that the period of the wave displacements is $P = 2\pi a/(c - \bar{u}) \approx 10^6$ s for both the Kelvin and Rossby modes. Unless the chemical lifetime of the absorber at the cloud tops is shorter than this, the effective horizontal and vertical diffusion times must be longer to explain the long lifetime of the large-scale features in the images. For planetary-scale motions with length scale $L = k^{-1} = a$, this then implies an upper limit for the horizontal diffusivity $\kappa_H = a^2/P \approx 4 \times 10^7$ m^2 s^{-1}. The persistence of large-scale UV features for at least a year in the near absence of wave activity (1982–83) implies that the actual diffusivity may be even lower, $\kappa_H \approx 10^6$ m^2 s^{-1}. By comparison, Del Genio and Suozzo (1987) estimated $\kappa_H \approx 10^7$ m^2 s^{-1} for the large-scale eddies in their slow rotation GCM experiment. The vertical diffusion time in the presence of the waves has been estimated previously from photochemical and turbulence estimates of κ_v as $\tau_m = (\kappa_v \mu^2)^{-1} \approx 10^6$ s, comparable to the period of wave displacements. After wave activity ceases, a more appropriate estimate might be $H^2/\kappa_v \approx 10^7$ s, which is marginally consistent with the observed lifetime of the large-scale features. The advection time scale for the cloud level Hadley circulation is 10^6–10^7 s, based on

a mean meridional wind of 2–5 m s^{-1} (Rossow et al. 1989). This may explain why the signature of the equatorial wave in the UV brightness field spreads globally after its initial appearance; e.g., from spring 1979 to spring 1980 (Fig. 1).

5. Solar-locked variations

The waves we have discussed thus far are transient in nature, propagating with respect to the mean flow and the surface of Venus. It is also possible to look for stationary waves in the OCPP data by averaging the data with respect to a different fixed coordinate system. We have not found any evidence for systematic variations with longitude in a coordinate system fixed to the solid planet, although the observational constraints of the OCPP experiment limit our ability to detect such waves. However, stationary oscillations in a solar-fixed reference frame are present in both the UV brightness and cloud-tracked wind data.

Figure 12 shows the distribution of zonal and meridional winds in the solar-fixed reference frame for the spring 1982 epoch. Zonal winds are a minimum approximately one hour before local noon and increase by about 10 m s^{-1} across the afternoon quadrant, the solar-fixed structure being most obvious at low latitudes. Meridional winds peak about one hour after local noon (poleward) and in the early morning (equatorward), with the solar-fixed component most evident away from the equator. These features are similar to those deduced by Limaye (1988) from manual cloud-tracked OCPP winds and consistent with spatial structure observed during Mariner 10 (Limaye and Suomi 1981). The solar-fixed wind is more symmetric about the subsolar meridian in 1979 and 1985; in 1983, the zonal wind minimum occurs slightly after local noon (Rossow et al. 1989).

We see less than 180° of longitude in the OCPP images, so it is impossible to define the amplitude of these variations or definitively associate them with solar thermal tides, nor can we diagnose the particular harmonic responsible for most of the variance. Uncertainty about the precise level of the UV features and the width of the OCPP weighting function precludes detailed comparisons with a tidal model. With these considerations in mind, we can say that the zonal wind observations are broadly consistent with calculations of the semidiurnal tide performed by Pechmann (1983). Pechmann's model predicts a semidiurnal zonal wind amplitude of 5–10 m s^{-1} and peak zonal winds near dawn and dusk in the 65–70 km altitude region at the equator, with the phase shifting slightly to earlier local time with increasing latitude. The phase varies rapidly with height in this model, so the OCPP data do not provide a sensitive test—the observed longitudinal structure can be made consistent with the model merely by choosing an appropriate altitude. The model also predicts maximum midlatitude meridional winds shortly after local noon, in agreement with the image data.

The observed winds are also consistent with the expected structure of the diurnal tide on Venus. Pechmann explained the dominance of the semidiurnal signal in the OIR data in part as a consequence of the short diurnal vertical wavelength, which causes the diurnal signal to smear out when convolved with the broad OIR weighting function. However, the OCPP weighting function is apparently narrower than that of the OIR, given our estimate of the vertical wavelength of the Kelvin wave seen in the UV. Since the vertical wavelength of the diurnal tide is only slightly smaller than that of the Kelvin wave, the diurnal harmonic may therefore contribute more to the solar-fixed OCPP wind pattern than it does to the solar-fixed OIR temperature field. In our companion paper (Rossow et al. 1989) we in fact argue that the diurnal tide is comparable to or stronger than the semidiurnal tide at the UV cloud level and accounts for much of the morning–afternoon asymmetry and temporal variation of the solar-fixed wind field.

One puzzling feature of the observed winds is their apparent hemispheric asymmetry, with the minimum zonal wind occurring at 15°S rather than the equator at all local solar times. This behavior persists in subsets of the data acquired when the spacecraft was located over the equator. Thus, the asymmetry is real, and not simply an artifact of the OCPP viewing geometry (Rossow et al. 1989). Hemispheric asymmetry is also a ubiquitous feature of the mean meridional wind profile. This asymmetry argues against the wisdom of combining data from different hemispheres in analyses of the cloud level dynamics.

Solar-fixed structure is also evident in the normalized UV brightness patterns (Fig. 13). At low latitudes, the dominant feature is a minimum in brightness near local noon. At least part of this must be an artifact of variable scattering geometry across the disk. At 8:00 a.m. and 4:00 p.m., for example, the cosine of the solar zenith angle is 0.5; if we see down to $\tau \approx 4$ at nadir, we only see to $\tau \approx 2$ (several kilometer higher) at the earlier and later times for similar observer zenith angles. A small part of the longitudinal component of the solar-fixed wind field may also be an artifact for the same reason.

Superimposed on this pattern, though, is a slight but real morning–afternoon asymmetry, the afternoon side of the planet being darker than the morning side. This tendency accounts in part for the higher contrast of afternoon images compared to those acquired at similar phase angles in the morning (Rossow et al. 1980). There are two possible explanations for this behavior. OCPP polarimetry data imply greater optical thickness of the bright submicron haze near the morning terminator than near the evening terminator (Kawabata et al. 1980). The increasing zonal wind from morning to afternoon also implies divergence and thus

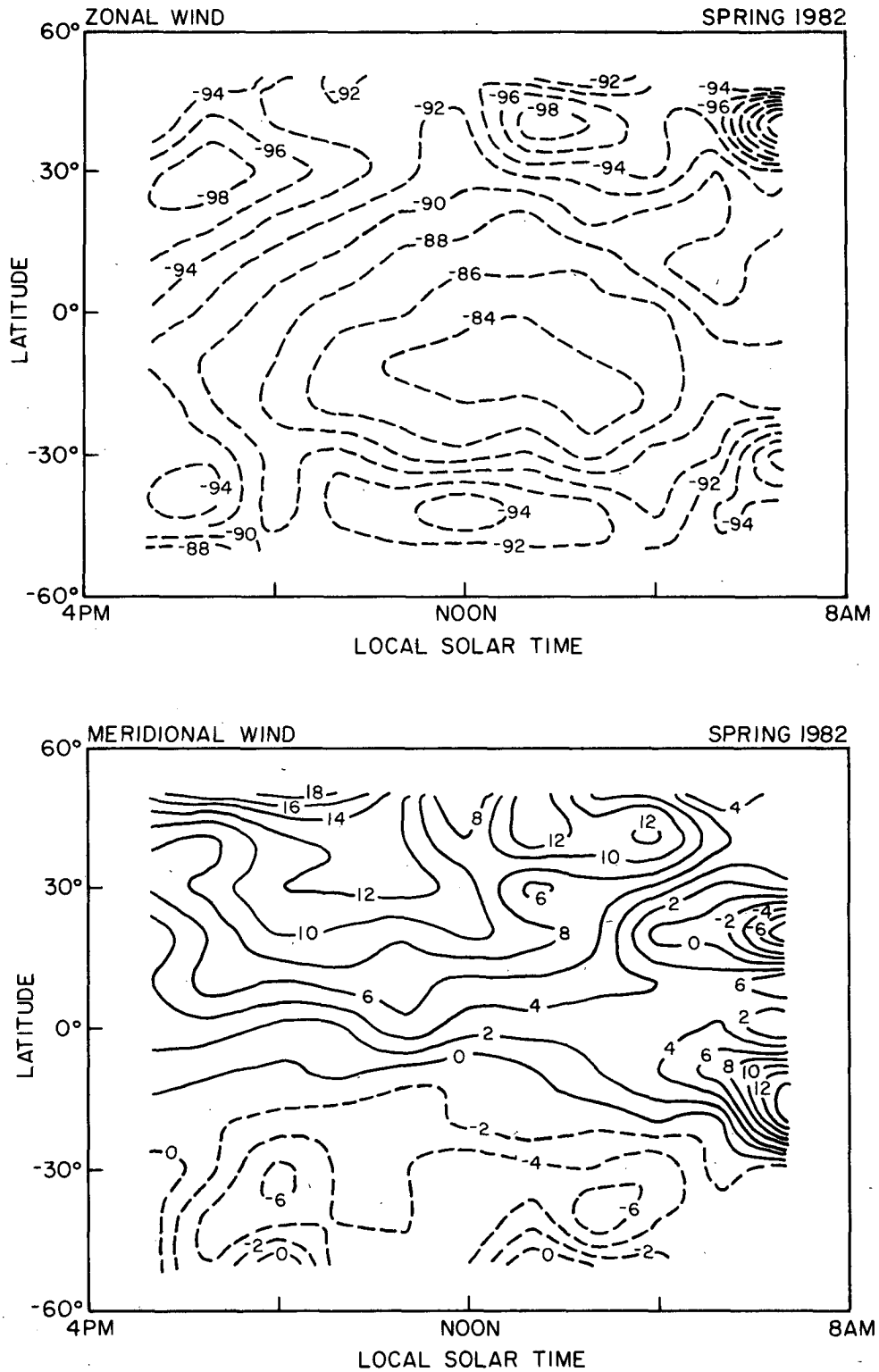

FIG. 12. Mean cloud-tracked zonal (upper) and meridional (lower) winds ($m\ s^{-1}$) in a solar-fixed coordinate system for the spring 1982 epoch. The subsolar longitude is at the center. The contour interval is 2 $m\ s^{-1}$.

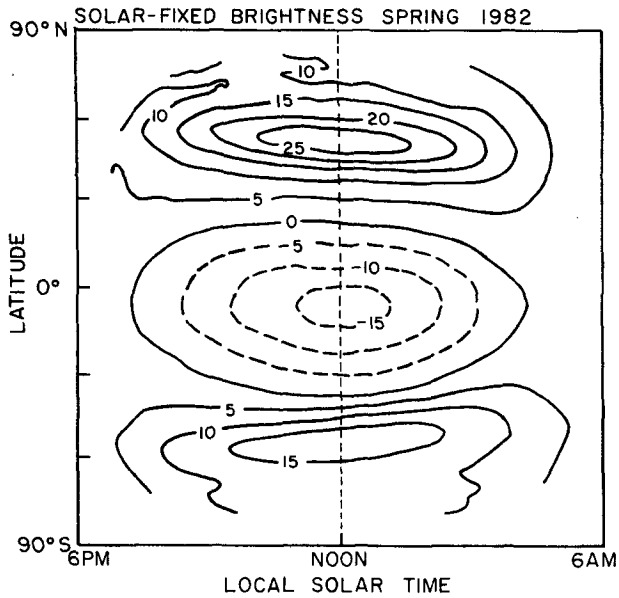

FIG. 13. As in Fig. 12 but for the solar-fixed normalized UV brightness distribution. The contour interval is 5 normalized data numbers.

vertical motion in the subsolar region. If upwelling produces dark features as we have suggested, then the subsolar region and areas downstream might be locations of an enhanced cloud level Hadley circulation. This is consistent with the early afternoon maximum in meridional wind (Fig. 12; see also Rossow et al. 1989). The solar-fixed brightness pattern varies less from one epoch to another than does the solar-fixed wind.

There is also a significant solar-fixed brightness component in midlatitudes. Aside from a subsolar longitude peak in brightness, which may also be a scattering geometry effect, there is a noticeable tilt in the bright polar band in each hemisphere. The band position moves from about 45° latitude early in the morning quadrant to 55° in the late afternoon, comparable to the amplitude of the transient 5-day oscillation discussed in the previous section. The tendency of meridional winds to increase from morning to early afternoon provides a natural explanation for this tilt.

If the brightness of the polar bands is an indication of local convergence and downwelling, then the bands are probably a tracer of the latitudinal extent of the cloud level Hadley cell. If this is the case, the Hadley cell does not extend all the way to the pole, as is often assumed for a slowly rotating planet. This conclusion is supported by the observation of a baroclinic zone of sharp temperature gradients at and above these altitudes poleward of 55° and an associated jet (Schofield and Taylor 1983; Newman et al. 1984; Walterscheid et al. 1985). A narrower Hadley cell might indicate that the mean meridional circulation is sensitive to the local atmospheric rotation rate in a superrotating atmosphere. Alternatively, the poleward extent may be determined primarily by the local eddy flux convergences (cf. Del Genio and Suozzo 1987), which are poorly constrained for Venus.

6. Discussion

We have diagnosed four distinct types of planetary-scale waves as common features of the Pioneer Venus OCPP images—transient Kelvin and Rossby–Haurwitz waves and diurnal and semidiurnal thermal tides. How important is each to the maintenance of the equatorial superrotation? The semidiurnal thermal tide has been extensively studied in recent years; estimates from a wave–mean flow interaction model (Baker and Leovy 1987) suggest that it contributes a maximum equatorial acceleration of about 0.2–0.3 m s^{-1} d^{-1} at an altitude several km below that seen in the images. The peak equatorial wind in this model is 5–10 m s^{-1} faster with the tide than without it, but most of the wind is a remnant of an imposed initial superrotation. The steady-state effect of the tide may be larger or smaller than this, since the model was not run to equilibrium.

The coincidence of the 4-day Kelvin wave's presence or absence and 5–10 m s^{-1} fluctuations in the mean cloud level equatorial wind suggest that it could play a role comparable to that of the tides in maintaining the superrotation. Indeed, according to our estimates the Kelvin wave and the semidiurnal tide have similar amplitudes. How does the Kelvin wave accelerate the wind? For a wave generated at depth, critical level absorption below the UV cloud level is not a factor, because the phase speed exceeds the mean wind speed at all altitudes from the surface to cloud top. A critical layer above cloud top cannot strictly be ruled out but seems unlikely if the sense of decreasing wind with height in the low-latitude thermal wind reconstructions holds to the equator.

Thermal and viscous dissipation are a more probable cause of the eddy flux convergence. A rough estimate of the penetration depth above the level at which damping becomes important is $D = c_{gz}/(\tau_r^{-1} + \tau_m^{-1})$, where $c_{gz} = \partial\omega/\partial\mu$ is the vertical group velocity (cf. Baker and Leovy 1987). For simplicity we neglect the damping contribution to the dispersion relation in the computation of c_{gz}; from (2) we thus estimate $\mu \approx -N/(c - \bar{u}) = -Nk/\omega$ and

$$D = \frac{\partial\omega}{\partial\mu}(\tau_r^{-1} + \tau_m^{-1})^{-1} \approx \frac{Nk}{\mu^2(\tau_r^{-1} + \tau_m^{-1})}. \quad (9)$$

With τ_r = 4 days, τ_m = 20 days, and λ_z = 11 km we get D = 2.3 km. This suggests that the Kelvin wave cannot propagate too far above the UV cloud level without depositing significant momentum, primarily because of radiative damping. In fact, thermal dissipation may be even more efficient than our Newtonian cooling estimate, because slightly more solar flux is absorbed in dark UV features, which are cold (Fig. 9). In other words, UV albedo variations may cause the

altitude of peak wave forcing of the zonal flow to coincide with the level of peak solar flux deposition.

Momentum deposition by wave breaking may also be possible. There is considerable controversy in the current literature over the appropriate conditions for and the effects of breaking. We will make a crude estimate based on the simple parameterization of Lindzen (1981), which predicts breaking when the wave amplitude becomes large enough to make the local lapse rate statically unstable, i.e., when $-\Gamma + dT'/dz < -\Gamma_d$, where Γ is the mean lapse rate and Γ_d the dry adiabatic lapse rate. For a monochromatic sinusoidal perturbation in the absence of large zonal wind curvature in z, Lindzen's criterion can be used to define the breaking level as

$$z_b = 2H \ln\left(\frac{N\lambda_z}{2\pi|u'|}\right), \tag{10}$$

where z_b is measured upward from the level seen in the images. For the diagnosed Kelvin wave parameters, $z_b \approx 3.7H \approx 19$ km. This suggests that thermal and viscous dissipation are more important than breaking. However, nonlinearities may cause momentum deposition to begin below the nominal breaking level. The images themselves actually suggest that breaking may sometimes occur near the visible cloud level—mesoscale cellular features reminiscent of convective structures exist primarily where large-scale dark material is present (Del Genio and Rossow 1982, Fig. 5). Since dark features are cold (Fig. 9), even with damping taken into account, this is precisely the location where destabilization by the wave is a maximum. Young (1975) could not detect a CO_2 rotational temperature difference between bright and dark markings but noted a much greater temperature variance in dark features; convection provides a ready explanation for this observation. Furthermore, convection provides another means for bringing dark material up to the visible cloud level. Given its short time scale compared to the slow large-scale upwelling associated with the wave itself, convection may be partly responsible for maintaining the integrity of the UV features against diffusion.

We can estimate the cloud level acceleration of the wind by distributing the Kelvin wave vertical eddy momentum flux over a distance Δz:

$$\frac{\partial \bar{u}}{\partial t} \approx \frac{\overline{u'w'}}{\Delta z} \approx \frac{|u'|^2\lambda_z}{\Delta z \lambda_x}. \tag{11}$$

If $\Delta z = H$ as suggested by Lindzen for breaking, $\partial\bar{u}/\partial t \approx 0.1$ m s^{-1} d^{-1} and is roughly constant above z_b in the absence of a critical level. For thermal and mechanical dissipation $\Delta z = D$, giving $\partial\bar{u}/\partial t \approx 0.2$ m s^{-1} d^{-1} concentrated near the cloud top. Thus, the Kelvin wave's acceleration of the zonal wind is comparable to that estimated for the semidiurnal tide and is certainly capable of explaining a 10 m s^{-1} increase in the equatorial zonal wind over two years (Fig. 6). That Kelvin waves should be important to the momentum balance is not surprising in light of their apparently central role in the dynamics of the terrestrial stratosphere (cf. Holton and Lindzen 1972; Hitchman and Leovy 1988). The potential role of Kelvin waves on Venus was first suggested in Leovy's (1973) note on cyclostrophic balance.

The 5-day midlatitude wave also appears to be of large enough amplitude to affect the momentum balance. The wave has characteristics consistent with vertical propagation of a neutral Rossby wave. The breaking level for this wave, from (10), is 85–90 km. Its presence in all the OIR channels implies that there is no critical level between the cloud top and this altitude, and therefore that $\bar{u} \gtrsim 60$ m s^{-1} in this region in midlatitudes. This is consistent with the zonal wind structure deduced by Fels et al. (1984) from comparison of a tidal model to OIR observations. It also agrees with the thermal wind profile up to about 80 km; above this level, cyclostrophy breaks down (Newman et al. 1984), implying that eddies are important to the momentum balance there. The dissipation penetration depth $D \gg H$ for this wave. Thus, any vertical eddy flux convergence by dissipation or breaking of the Rossby wave probably occurs well above cloud top. If the wave is generated at cloud level, it may affect the momentum balance there either by the divergence of the resulting vertical eddy flux or by its meridional fluxes.

Barotropic instability of the midlatitude jet is a likely mechanism for producing eddies in this location (Rossow and Williams 1979). This process is ubiquitous at midlatitudes in all slowly rotating general circulation models (GCMs) (Rossow 1983; Covey et al. 1986a; Del Genio and Suozzo 1987; Williams 1988). Analysis of the Mariner 10 zonal wind profile suggests that wavenumbers 2–4 and 7–11 are barotropically unstable (Travis 1978). Our longitudinal averaging procedure precludes detection of such waves. However, in the mature phase of such a disturbance, we would expect a nonlinear cascade of energy to produce wavenumber 1 neutral Rossby–Haurwitz waves similar to those we have diagnosed. Barotropic instability may be sporadic and hemispherically asymmetric on Venus if the forcing is weak. This is suggested by the shape of the mean zonal wind profile and the latitudinal variation of higher wavenumber eddy components of the flow (Rossow et al. 1989). However, the symmetric mode is preferred in a weakly forced flow with net angular momentum (Rossow and Williams 1979). Linear stability analyses (Kuo 1978) and GCM simulations (Rossow 1983) indicate that, in three dimensions, barotropic instability produces significant vertical as well as horizontal eddy momentum transports and substantial baroclinic conversion above the jet level. These waves may therefore affect both the wind and the temperature field in the Venus upper atmosphere.

One problem with this interpretation is the inferred direction of the associated meridional momentum

fluxes. Since the equatorial side of the jet is barotropically unstable in Pioneer Venus data (Newman et al. 1984), equatorward eddy momentum fluxes would be expected at lower latitudes. Such behavior occurs in slowly rotating GCMs and is predicted by Kuo's (1978) stability analysis. However, the observed fluxes derived from cloud-tracked winds are weakly poleward in most epochs (Limaye et al. 1988; Rossow et al. 1989). There are several possible explanations for this difference. The measured eddy transport is highly uncertain because of sparse sampling, possible dayside biases, and possible confusion of time variations of the mean flow with wave motions. The sporadic nature of the instability may require extensive observations to detect the dynamically important transports; equatorward transports do occur, e.g., in midlatitudes in spring 1985 when the 5-day wave is apparently growing. Alternatively, the vertically integrated eddy flux may be equatorward but change sign with altitude, as is the case in slow rotation GCM simulations (Rossow 1983; Del Genio et al. 1987). In this event, equatorward fluxes may exist at the jet level but not elsewhere. The primary jet in the thermal wind data occurs near 70 km, about a scale height above the level seen in the UV images. Thus, eddy fluxes derived from cloud-tracked winds may not be indicative of the vertically integrated momentum balance. Beneath the visible cloud level (60 km altitude), a secondary high latitude jet is suggested in cyclostrophic thermal winds (Newman et al. 1984). If this feature is real, it too may be a source of quasi-barotropic eddies. The 5-day wave has a critical level in the vicinity of the middle cloud layer, so it can be generated at any higher altitude and still propagate up to cloud top.

Our impression from analysis of the solar-fixed wind field is that the amplitude of the semidiurnal tidal harmonic is relatively constant, while that of the diurnal tide varies considerably between epochs (Rossow et al. 1989). The diurnal tide is apparently strongest in spring 1982, when the mean zonal wind at the equator is weakest. If the eddy–mean flow interaction time is short compared to the 5–10 year vacillation time scale, the diurnal tide may therefore act as a *sink* for the zonal wind at the UV cloud level. If so, this would be a significant advance in our understanding of the momentum balance, since most previous studies have considered only possible *sources* of cloud top momentum and have used only ad hoc sinks. Since diurnal radiative forcing is expected to vary on a longer time scale than the 1–2 years over which tidal amplitude variations occur, the tidal variation is best explained as an effect of the varying mean wind and/or static stability on its vertical propagation characteristics.

The overriding question raised by our analysis is: What causes the Venus cloud level dynamics to vacillate on the 5–10 year time scale? The answer depends on the forcing mechanism responsible for the Kelvin wave. On Earth, the generation mechanism for Kelvin waves is still quite uncertain. Land–ocean contrasts and sea surface temperature patterns, which organize tropical moist convection on the planetary scale, are one possibility (Hayashi and Golder 1978), but it is not obvious how dry convection on Venus could be modulated in an analogous fashion (except by the wave itself).

Covey and Schubert (1982) showed that the Kelvin wave is a preferred cloud level response to white noise forcing at any level below cloud top. They suggested that the observed 4-day wave might reflect primarily the filtering of other frequencies by the Venus wind and static stability profiles rather than preferential forcing at 4 days. We might then speculate that the presence of two wave modes at cloud top, one faster and one slower than the mean wind, constrains the magnitude of the mean wind to lie between the phase speeds of the two waves. Covey and Schubert noted, however, that phase speeds faster than that observed were preferred in their model, suggesting that "red noise" forcing may be necessary. There was also no preference for wavenumber 1 in that study. Thus, the observed Kelvin wave scale may be the result of a nonlinear cascade to low wavenumbers, as occurs in two-dimensional flow (cf. Rossow and Williams 1979) and in GCM simulations at slow rotation (cf. Del Genio and Suozzo 1987).

Recent analyses of data from the First GARP Global Experiment have suggested that the terrestrial stratospheric Kelvin wave is forced laterally by the meridional convergence of wave energy flux from higher latitudes (Lu and Yanai 1987). A similar mechanism might operate on Venus; the fact that the midlatitude 5-day wave and equatorial 4-day wave appear together as distinct entities in the same imaging epochs (1979, 1980, 1985) supports the speculation that the former may indirectly give rise to the latter.

The 5–10 year vacillation most likely reflects an internal nonlinear time scale related to wave–wave or wave–mean flow interactions within the cloud layer. Two such phenomena are important in the terrestrial upper atmosphere, and both involve Kelvin waves. The canonical example, the quasi-biennial oscillation (QBO) of the tropical stratosphere, is thought to be driven by dissipation and/or critical layer absorption of upward-propagating Kelvin and Yanai waves (cf. Holton and Lindzen 1972). It is not clear whether this mechanism is relevant to Venus. There is no evidence in our spectra for a Yanai wave, which transports retrograde (against the planet's rotation) momentum upward. However, on Earth, the Yanai wave is present primarily as wavenumber 4, and the longitudinal averaging procedure we employ on the OCPP data limits us to detecting wavenumbers 1 and 2. The Yanai wave is antisymmetric about the equator and therefore requires asymmetric forcing. While the predominant impression in the images is one of hemispheric symmetry (Figs. 1, 2), hints of antisymmetric behavior in

the cloud-tracked wind field exist (Rossow et al. 1989). Even though seasonality is nearly absent on Venus, some asymmetry may be produced if jet instabilities in the two hemispheres set in at different times. This is a common occurrence in slowly rotating GCMs.

A more useful analogy for Venus may be the semiannual oscillation (SAO) of temperature and wind, which peaks at the terrestrial stratopause and mesopause. The SAO appears to be the net result of a number of dynamical mechanisms (cf. Hamilton 1986; Hitchman and Leovy 1988): prograde acceleration by a dissipating "fast" Kelvin wave and breaking small-scale gravity waves and retrograde acceleration by equatorward propagation of extratropical planetary waves and the residual mean circulation. The SAO is not directly applicable to Venus, because its time scale is determined by seasonal forcing, but the Venus 5–10 year oscillation may well involve some of the same dynamical modes. If, for example, the Venus Kelvin wave is forced laterally by meridional eddy flux convergence from the barotropically unstable high-latitude jet at 60 km and transports this momentum to cloud top, the cloud level Hadley cell would return the momentum to midlatitudes. The transition to the quiescent state (i.e., 1982–83) might occur if equatorward barotropic eddy fluxes stabilize the high-latitude jet faster than its momentum can be resupplied, or if the Hadley cell flux convergence from above stabilizes the equatorward side of this jet.

The poleward eddy momentum flux seen in the cloud-tracked winds might be related to the tilt of the *Y*-feature and bow shapes prevalent in the images. The shape of these features resembles the eddy streamline pattern produced by a barotropically unstable equatorial jet, i.e., the tilt is opposite the sense of the jet angular velocity gradient. This configuration is required for poleward transport and conversion from mean to eddy kinetic energy. Two-dimensional simulations of slowly rotating atmospheres produce such waves in the presence of equatorial forcing (Rossow and Williams 1979). An equatorial maximum is not present in the mean flow, but transient structures of this nature are often seen (Rossow et al. 1989). The vertex of the *Y* and the afternoon quadrant may be favored locations for low-latitude barotropic instability because the Kelvin wave and thermal tide produce local wind maxima there. This explanation is consistent with several observations: 1) eddy fluxes are larger in 1979–80, when the Kelvin wave is present, than in 1982–83, when it is absent (Limaye et al. 1988; Rossow et al. 1989); and 2) Gaussian perturbations with $\theta_{e\text{-fold}} = 23°$ superimposed on the mean flow tend to be unstable poleward of 30° latitude, where maximum poleward eddy transport is observed. If low latitudes are barotropically stable, the tilted arms may instead be forced equatorial Rossby waves. In the presence of damping such waves have a poleward component of propagation and therefore a meridional tilt in the same sense as the arms of the *Y* (Chang and Lim 1982). The deceleration of the equatorial wind produced by the divergence of the observed flux can be estimated from Rossow et al. (1989) as

$$\frac{\partial \bar{u}}{\partial t} = -\frac{\partial}{\partial y}\overline{u'v'} \approx -\frac{30\ \mathrm{m^2\ s^{-2}}}{5000\ \mathrm{km}} \approx -0.5\ \mathrm{m\ s^{-1}\ d^{-1}}. \tag{12}$$

This is of the correct magnitude to balance the combined local acceleration due to the Kelvin wave and the thermal tide.

7. Conclusions

We have demonstrated that at least four planetary-scale wave modes exist at cloud levels in the Venus atmosphere and have suggested that all of them play an important role in the maintenance of the equatorial winds. The available evidence tentatively suggests that the equatorial dynamics is cyclic with an apparent time scale of 5–10 years. The key aspects of the Pioneer Venus dataset that made our analysis possible are its continuous imaging coverage over many months and the decadal monitoring provided by an orbiting spacecraft. Nonetheless, even this data sample is too limited to provide anything more than a lower limit for the time scale of the variability. Regardless of the exact time scale, our results argue forcefully against attempts to infer the mean state of a planet's atmosphere from isolated flyby observations.

The OCPP images and other Pioneer Venus instruments have documented the nature of the Venus superrotation and given us a clearer idea of its causes. Further observations are desperately needed for two reasons. The lifetime of the Pioneer Venus Orbiter is limited to 1993, but imaging opportunities beyond those discussed in this paper are unlikely. Consequently, a more accurate determination of the time scale for the oscillation of the equatorial wind awaits future spacecraft missions or a return to active Earth-based observing, neither of which is planned for the near future. The biggest limitation of existing Venus datasets is the paucity of information about the bulk of the atmosphere below cloud top. Most of the angular momentum of the atmosphere resides at depth, so a complete understanding of the superrotation necessitates monitoring the deep atmosphere. Even the cloud layer below the visible level is poorly sampled with the exception of radio occultation data.

One opportunity for enhancing our knowledge of Venus in the next few years is the Galileo spacecraft, which is scheduled to encounter Venus in 1990 as the first part of its VEEGA trajectory to Jupiter. There are severe budgetary constraints on the amount of data Galileo will be able to return from Venus, but a number of relevant observations are possible. High-resolution Solid State Imaging of the equatorial band, combined

with thermal data from the Photopolarimeter Radiometer, may help identify the mesoscale cellular features as convection and quantify the difference in temperature and temperature variance between large-scale dark and bright regions. North–south scans across the bright polar band with a number of instruments may provide clues about the relationships between cloud structure, temperature, and the meridional circulation in midlatitudes. The Near-Infrared Mapping Spectrometer may be able to probe some of the deeper levels largely inaccessible to *Pioneer Venus*; correlations of such data with imaging and radiometry of the cloud top could provide a more comprehensive picture of processes occurring within the cloud layer. Direct measurement of the three-dimensional dynamical fluxes is unlikely, though. The ultimate answers to the superrotation problem are therefore most likely to be obtained through fully nonlinear modeling of the slowly rotating dynamical regime. The role of the UV features in radiation/dynamics interactions at cloud top, and the dependence of the cloud level wind speed on the phase velocity of transient wave modes, are two especially intriguing areas for further investigation.

Acknowledgments. The authors are grateful to L. Travis and A. Young for helpful discussions. We also thank an anonymous referee for suggesting coherence analysis to support our identification of the UV features as wave motions. T. Eichler processed the cloud-tracked wind datasets used in this paper. G. Boult and J. Lee assisted in the reduction and analysis of UV brightness data. Drafting assistance was provided by L. Del Valle and J. Mendoza. This research was supported by the Pioneer Venus Project.

REFERENCES

Apt, J., and J. Leung, 1982: Thermal periodicities in the Venus atmosphere. *Icarus,* **49,** 423–427.

Baker, N. L., and C. B. Leovy, 1987: Zonal winds near Venus' cloud top level: A model study of the interaction between the zonal mean circulation and the semidiurnal tide. *Icarus,* **69,** 202–220.

Belton, M. J. S., 1982: An interpretation of the near-ultraviolet absorption spectrum of SO_2: Implications for Venus, Io, and laboratory measurements. *Icarus,* **52,** 149–165.

——, G. R. Smith, G. Schubert and A. D. Del Genio, 1976: Cloud patterns, waves and convection in the Venus atmosphere. *J. Atmos. Sci.,* **33,** 1394–1417.

Boyd, J. P., 1978: The effects of latitudinal shear on equatorial waves. Part I: Theory and methods. *J. Atmos. Sci.,* **35,** 2236–2258.

Chang, C.-P., 1977: Viscous internal gravity waves and low-frequency oscillations in the tropics. *J. Atmos. Sci.,* **34,** 901–910.

——, and H. Lim, 1982: On the effects of viscous damping on equatorial Rossby waves. *J. Atmos. Sci.,* **39,** 1726–1733.

Coffeen, D. L., and J. E. Hansen, 1974: Polarization studies of planetary atmospheres. *Planets, Stars and Nebulae Studied with Photopolarimetry,* T. Gehrels, Ed., University of Arizona Press, 518–581.

Counselman, C. C. III, S. A. Gourevitch, R. W. King and G. B. Loriot, 1980: Zonal and meridional circulation of the lower atmosphere of Venus determined by radio interferometry. *J. Geophys. Res.,* **85,** 8026–8030.

Covey, C., and G. Schubert, 1982: Planetary-scale waves in the Venus atmosphere. *J. Atmos. Sci.,* **39,** 2397–2413.

——, E. J. Pitcher and J. P. Brown, 1986: General circulation model simulations of superrotation in slowly rotating atmospheres: Implications for Venus. *Icarus,* **66,** 380–396.

——, R. L. Walterscheid and G. Schubert, 1986: Dissipative tides: Application to Venus' lower atmosphere. *J. Atmos. Sci.,* **43,** 3273–3278.

Crisp, D., 1989: Radiative forcing of the Venus mesosphere. II. Thermal fluxes, cooling rates, and radiative equilibrium temperatures. *Icarus,* **77,** 391–413.

——, and A. T. Young, 1978: Vertical extent of zonal winds on Venus. *Icarus,* **35,** 182–188.

Del Genio, A. D., and W. B. Rossow, 1982: Temporal variability of ultraviolet cloud features in the Venus stratosphere. *Icarus,* **51,** 391–415.

——, and R. J. Suozzo, 1987: A comparative study of rapidly and slowly rotating dynamical regimes in a terrestrial general circulation model. *J. Atmos. Sci.,* **44,** 973–986.

——, J. A. Thorburn, R. J. Suozzo and W. B. Rossow, 1987: Equatorial superrotation in a slowly rotating GCM by the Gierasch mechanism: Implications for Venus and Titan. *Bull. Amer. Astron. Soc.,* **19,** 865.

Dollfus, A., 1975: Venus: Evolution of the upper atmospheric clouds. *J. Atmos. Sci.,* **32,** 1060–1070.

Elson, L., 1983: Solar related waves in the Venusian atmosphere from the cloud tops to 100 km. *J. Atmos. Sci.,* **40,** 1535–1551.

Esposito, L. W., 1980: Ultraviolet contrasts and the absorbers near the Venus cloud tops. *J. Geophys. Res.,* **85,** 8151–8157.

——, and L. D. Travis, 1982: Polarization studies of the Venus UV contrasts: Cloud height and haze variability. *Icarus,* **51,** 374–390.

Fels, S. B., and R. S. Lindzen, 1974: The interaction of thermally excited gravity waves with mean flows. *Geophys. Fluid Dyn.,* **6,** 149–191.

——, J. T. Schofield and D. Crisp, 1984: Observations and theory of the solar semidiurnal tide in the mesosphere of Venus. *Nature,* **312,** 431–434.

Gierasch, P. J., 1975: Meridional circulation and the maintenance of the Venus atmospheric rotation. *J. Atmos. Sci.,* **32,** 1038–1044.

——, 1987: Waves in the atmosphere of Venus. *Nature,* **328,** 510–512.

Gossard, E. E., and W. H. Hooke, 1975: *Waves in the Atmosphere.* Elsevier, 456 pp.

Hamilton, K., 1986: Dynamics of the stratospheric semiannual oscillation. *J. Meteor. Soc. Japan,* **64,** 227–244.

Hansen, J. E., and J. W. Hovenier, 1974: Interpretation of the polarization of Venus. *J. Atmos. Sci.,* **31,** 1137–1160.

Hartley, K. H., A. R. Wolff and L. D. Travis, 1989: Croconic acid: An absorber in the Venus clouds? *Icarus,* **77,** 382–390.

Hayashi, Y., and D. G. Golder, 1978: The generation of equatorial transient planetary waves: Control experiments with a GFDL general circulation model. *J. Atmos. Sci.,* **35,** 2068–2082.

Hitchman, M. H., and C. B. Leovy, 1988: Estimation of the Kelvin wave contribution to the semiannual oscillation. *J. Atmos. Sci.,* **45,** 1462–1475.

Holton, J. R., and R. S. Lindzen, 1972: An updated theory for the quasi-biennial oscillation of the tropical stratosphere. *J. Atmos. Sci.,* **29,** 1076–1080.

Kawabata, K., D. L. Coffeen, J. E. Hansen, W. A. Lane, M. Sato and L. D. Travis, 1980: Cloud and haze properties from Pioneer Venus polarimetry. *J. Geophys. Res.,* **85,** 8129–8140.

Kerzhanovich, V. V., and M. Ya. Marov, 1983: The atmospheric dynamics of Venus according to Doppler measurements by the *Venera* entry probes. Venus, D. M. Hunten, L. Colin, T. M. Donahue and V. I. Moroz, Eds., University of Arizona Press, 766–778.

Kliore, A. J., and I. R. Patel, 1980: The vertical structure of the atmosphere of Venus from Pioneer Venus orbiter radio occultations. *J. Geophys. Res.,* **85,** 7957–7962.

Knollenberg, R. G., L. Travis, M. Tomasko, P. Smith, B. Ragent, L. Esposito, D. McCleese, J. Martonchik and R. Beer, 1980: The

clouds of Venus: A synthesis report. *J. Geophys. Res.*, **85,** 8059–8081.

Kuo, H. L., 1978: A two-layer model study of the combined barotropic and baroclinic instability in the tropics. *J. Atmos. Sci.*, **35,** 1840–1860.

Leovy, C. B., 1973: Rotation of the upper atmosphere of Venus. *J. Atmos. Sci.*, **30,** 1218–1220.

——, 1987: Zonal winds near Venus' cloud top level: An analytic model of the equatorial wind. *Icarus,* **69,** 193–201.

Limaye, S. S., 1985: Venus atmospheric circulation: Observations and implications of the thermal structure. *Adv. Space Res.*, **5,** 51–62.

——, 1988: Venus: Cloud level circulation during 1982 as determined from Pioneer Cloud Photopolarimeter images. II. Solar longitude dependent circulation. *Icarus,* **73,** 212–226.

——, and V. E. Suomi, 1981: Cloud motions on Venus: Global structure and organization. *J. Atmos. Sci.*, **38,** 1220–1235.

——, C. J. Grund and S. P. Burre, 1982: Zonal mean circulation at the cloud level on Venus: Spring and fall 1979 OCPP observations. *Icarus,* **51,** 416–439.

——, C. Grassotti and M. J. Kuetemeyer, 1988: Venus: Cloud level circulation during 1982 as determined from Pioneer Cloud Photopolarimeter images. I. Time and zonally averaged circulation. *Icarus,* **73,** 193–211.

Lindzen, R. S., 1981: Turbulence and stress due to gravity wave and tidal breakdown. *J. Geophys. Res.*, **86,** 9707–9714.

Longuet-Higgins, M. S., 1968: The eigenfunctions of Laplace's tidal equations over a sphere. *Phil. Trans. Roy. Soc. London,* **A262,** 511–607.

Lu, M.-M., and M. Yanai, 1987: Excitation mechanisms of equatorially trapped waves and the tropical low-frequency oscillation during the special observing periods of FGGE. *Preprints, 17th Conf. on Hurricanes and Tropical Meteorology,* Miami, Amer. Meteor. Soc., 397–400.

Newman, M. E., G. Schubert, A. J. Kliore and I. Patel, 1984: Zonal winds in the middle atmosphere of Venus from Pioneer Venus radio occultation data. *J. Atmos. Sci.*, **41,** 1901–1913.

Pechmann, J. B., 1983: Thermal tides in the atmosphere of Venus. Ph.D. thesis, California Institute of Technology, 286 pp.

——, and A. P. Ingersoll, 1984: Thermal tides in the atmosphere of Venus: Comparison of model results with observations. *J. Atmos. Sci.*, **41,** 3290–3313.

Preston, R. A., C. E. Hildebrand, G. H. Purcell, J. Ellis, C. T. Stelzried, S. G. Finley, R. Z. Sagdeev, V. M. Linkin, V. V. Kerzhanovich, V. I. Altunin, L. R. Kogan, V. I. Kostenko, L. I. Matveenko, S. V. Pogrebenko, I. A. Strukov, E. L. Akim, Yu. N. Alexandrov, N. A. Armand, R. N. Bakitko, A. S. Vyshlov, A. F. Bogomolov, Yu. N. Gorchankov, A. S. Selivanov, N. M. Ivanov, V. F. Tichonov, J. E. Blamont, L. Boloh, G. Laurans, A. Boischot, F. Biraud, A. Ortega-Molina, C. Rosolev and G. Petit, 1986: Determination of Venus winds by ground-based radio tracking of the VEGA balloons. *Science,* **231,** 1414–1416.

Rossow, W. B., 1978: Cloud microphysics: Analysis of the clouds of Earth, Venus, Mars, and Jupiter. *Icarus,* **36,** 1–50.

——, 1983: A general circulation model of a Venus-like atmosphere. *J. Atmos. Sci.*, **40,** 273–302.

——, 1985: Atmospheric circulation of Venus. *Adv. Geophys.*, **28A,** 347–379.

——, and G. P. Williams, 1979: Large-scale motion in the Venus stratosphere. *J. Atmos. Sci.*, **36,** 377–389.

——, A. D. Del Genio, S. S. Limaye, L. D. Travis and P. H. Stone, 1980: Cloud morphology and motions from Pioneer Venus images. *J. Geophys. Res.*, **85,** 8107–8128.

——, A. D. Del Genio and T. P. Eichler, 1989: Cloud-tracked winds from Pioneer Venus images. *J. Atmos. Sci.*, submitted.

Schofield, J. T., and F. W. Taylor, 1983: Measurements of the mean, solar-fixed temperature and cloud structure in the middle atmosphere of Venus. *Quart. J. Roy. Meteor. Soc.*, **109,** 57–80.

Taylor, F. W., R. Beer, M. T. Chahine, D. J. Diner, L. S. Elson, R. D. Haskins, D. J. McCleese, J. V. Martonchik, P. E. Reichley, S. P. Bradley, J. Delderfield, J. T. Schofield, C. B. Farmer, L. Froideveaux, J. Leung, M. T. Coffey and J. C. Gille, 1980: Structure and meteorology of the middle atmosphere of Venus: Infrared remote sensing from the Pioneer orbiter. *J. Geophys. Res.*, **85,** 7963–8006.

Thompson, P. D., 1948: The propagation of permanent-type waves in horizontal flow. *J. Meteor.*, **5,** 166–168.

Thompson, R. O. R. Y., 1979: Coherence significance levels. *J. Atmos. Sci.*, **36,** 2020–2021.

Toon, O. B., R. P. Turco and J. B. Pollack, 1982: The ultraviolet absorber on Venus: Amorphous sulfur. *Icarus,* **51,** 358–373.

Travis, L. D., 1975: On the origin of the ultraviolet contrasts on Venus. *J. Atmos. Sci.*, **21,** 1190–1200.

——, 1978: Nature of the atmospheric dynamics on Venus from power spectrum analysis of Mariner 10 images. *J. Atmos. Sci.*, **35,** 1584–1595.

——, 1979: Imaging and polarimetry with the Pioneer Venus Orbiter cloud photopolarimeter. *Proc. Soc. Photo.-Opt. Instrum. Eng.*, **183,** 299–304.

——, D. L. Coffeen, J. E. Hansen, K. Kawabata, A. A. Lacis, W. A. Lane, S. S. Limaye, W. B. Rossow and P. H. Stone, 1979: Orbiter cloud photopolarimeter investigation. *Science,* **208,** 781–785.

——, M. Sato and K. Kawabata, 1989: Polarimetric determination of the characteristics and variation of the polar haze on Venus. *Icarus,* submitted.

von Zahn, U., S. Kumar, H. Niemann and R. Prinn, 1983: Composition of the Venus atmosphere. *Venus,* D. M. Hunten, L. Colin, T. M. Donahue and V. I. Moroz, Eds., University of Arizona Press, 299–403.

Wallace, J. M., and V. E. Kousky, 1968: Observational evidence of Kelvin waves in the tropical stratosphere. *J. Atmos. Sci.*, **25,** 900–907.

Walterscheid, R. L., G. Schubert, M. Newman and A. J. Kliore, 1985: Zonal winds and the angular momentum balance of Venus' atmosphere within and above the clouds. *J. Atmos. Sci.*, **42,** 1982–1990.

Williams, G. P., 1988: The dynamical range of global circulations—I. *Climate Dyn.*, **2,** 205–260.

Young, A. T., 1975: Is the four-day "rotation" of Venus illusory? *Icarus,* **24,** 1–10.

——, 1985: Sulfur recombination on Venus: Forget S_3 and S_4. *Bull. Amer. Astron. Soc.*, **17,** 720.

——, A. Woszczyk and L. G. Young, 1974: Spectroscopic observations of spatial and temporal variations on Venus. *Acta Astron.*, **24,** 55–68.

Young, R. E., and G. Schubert, 1973: Dynamical aspects of the Venus 4-day circulation. *Planet. Space Sci.*, **21,** 1563–1580.

——, R. L. Walterscheid, G. Schubert, A. Seiff, V. M. Linkin and A. N. Lipatov, 1987: Characteristics of gravity waves generated by surface topography on Venus: Comparison with the VEGA balloon results. *J. Atmos. Sci.*, **44,** 2628–2639.